Bioactive Materials 28 (2023) 227–242

Contents lists available at ScienceDirect

Bioactive Materials

journal homepage: www.keaipublishing.com/en/journals/bioactive-materials

Li–Mg–Si bioceramics provide a dynamic immuno-modulatory and repair-supportive microenvironment for peripheral nerve regeneration

Yiting Sun [c,1], Hongjian Zhang [b,d,1], Yu Zhang [a,1], Zheqi Liu [a], Dongming He [c], Wanlin Xu [a], Siyi Li [a], Chenping Zhang [a,*], Zhen Zhang [a,**]

[a] Department of Oral & Maxillofacial-Head & Neck Oncology, Shanghai Ninth People's Hospital, Shanghai Jiao Tong University School of Medicine, College of Stomatology, Shanghai Jiao Tong University, National Center for Stomatology, National Clinical Research Center for Oral Diseases, Shanghai Key Laboratory of Stomatology, Shanghai, 200011, China

[b] State Key Laboratory of High Performance Ceramics and Superfine Microstructure, Shanghai Institute of Ceramics, Chinese Academy of Sciences, Shanghai, 200050, China

[c] Department of Oral & Cranio-Maxillofacial Surgery, Shanghai Ninth People's Hospital, Shanghai Jiao Tong University School of Medicine, College of Stomatology, Shanghai Jiao Tong University, National Center for Stomatology, National Clinical Research Center for Oral Diseases, Shanghai Key Laboratory of Stomatology, Shanghai, 200011, China

[d] Center of Materials Science and Optoelectronics Engineering, University of Chinese Academy of Sciences, Beijing, 100049, China

ARTICLE INFO

Keywords:
Peripheral nerve regeneration
Bioceramics
Immuno-modulation microenvironment
Macrophage
Nerve guidance conduit

ABSTRACT

Biomaterials can modulate the local immune and repair-supportive microenvironments to promote peripheral nerve regeneration. Inorganic bioceramics have been widely used for regulating tissue regeneration and local immune response. However, little is known on whether inorganic bioceramics can have potential for enhancing peripheral nerve regeneration and what are the mechanisms underlying their actions. Here, the inorganic lithium-magnesium-silicon (Li–Mg–Si, LMS) bioceramics containing scaffolds are fabricated and characterized. The LMS-containing scaffolds had no cytotoxicity against rat Schwann cells (SCs), but promoted their migration and differentiation towards a remyelination state by up-regulating the expression of neurotrophic factors in a β-catenin–dependent manner. Furthermore, using single cell-sequencing, we showed that LMS-containing scaffolds promoted macrophage polarization towards the pro-regenerative M2-like cells, which subsequently facilitated the migration and differentiation of SCs. Moreover, implantation with the LMS-containing nerve guidance conduits (NGCs) increased the frequency of M2-like macrophage infiltration and enhanced nerve regeneration and motor functional recovery in a rat model of sciatic nerve injury. Collectively, these findings indicated that the inorganic LMS bioceramics offered a potential strategy for enhancing peripheral nerve regeneration by modulating the immune microenvironment and promoting SCs remyelination.

1. Introduction

Peripheral nerve injury (PNI) can lead to the dysfunctions of sensory and motor nerves, and neuropathic pain, which remains a major clinical concern [1,2]. Following PNI, the injured nerves will be repaired by spontaneous self-healing process. However, such nerves repair has inherent limitation and incomplete with a poor functional recovery. Hence, the repairment of nerves after PNI continues to be a major challenge in the field of neurosurgery [3,4]. Autologous nerve graft (ANG) is the gold-standard method for bridging a long nerve gap (>5

Peer review under responsibility of KeAi Communications Co., Ltd.

* Corresponding author. Department of Oral & Maxillofacial-Head & Neck Oncology, Shanghai Ninth People's Hospital, Shanghai Jiao Tong University School of Medicine, College of Stomatology, Shanghai Jiao Tong University, National Center for Stomatology, National Clinical Research Center for Oral Diseases, Shanghai Key Laboratory of Stomatology, No.639, Zhi-zao-ju Road, Shanghai, 200011, China.

** Corresponding author. Department of Oral & Maxillofacial-Head & Neck Oncology, Shanghai Ninth People's Hospital, Shanghai Jiao Tong University School of Medicine, College of Stomatology, Shanghai Jiao Tong University, National Center for Stomatology, National Clinical Research Center for Oral Diseases, Shanghai Key Laboratory of Stomatology, No.639, Zhi-zao-ju Road, Shanghai, 200011, China.

E-mail addresses: zhang.chenping@163.com (C. Zhang), zz_nirvana@163.com (Z. Zhang).

[1] These authors contributed equally.

https://doi.org/10.1016/j.bioactmat.2023.05.013
Received 6 March 2023; Received in revised form 18 May 2023; Accepted 20 May 2023

mm). However, the availability of donor nerves is limited due to the loss of function at the donor site, neuroma formation, nerve distortion or dislocation, and mismatch in size between the donor and host nerves [2,5]. Hence, development of new tissue engineering strategies to promote peripheral nerve regeneration using biomaterial nerve guidance conduits (NGCs) in combination with cells, drugs, growth factors and others loaded as an alternative of ANG will be of great significance in management of PNI [6–8].

Successful biomaterial NGCs for peripheral nerve regeneration depends on the interaction of intricated NGCs with host's immune responses and Schwann cells (SCs) recruitment and differentiation [1,7,9]. Previous studies have showed that PNI can induce the de-differentiation of SCs in the ends of defect, leading to the production of chemokines that recruit immune cells into defect lesions for the clearance of debris [10,11]. Additionally, the NGC-grafts can induce innate immune responses in the body. During the process of immune responses to the grafted biomaterials, macrophages are the early infiltrates and crucial for biomaterial-mediated immune reactions. Macrophages can also transit immune response to tissue regeneration process, and modulation of macrophage activation and functions is crucial for the control of host responses to grafted biomaterials [12–14]. The high plasticity of macrophages makes them to be a potential target for promoting nerve regeneration. Furthermore, SCs are also critical for the process of peripheral nerve regeneration by switching from a proliferative, un-myelinating phenotype to re-myelinating phenotype [15–17]. Thus, the early-stage proliferation and late-stage remyelination of SCs are essential, but theoretically, these two biological processes can be mutually exclusive [16,18]. Therefore, the ability of promoting the dynamic functions of SCs during the nerve regenerative process is a critically design standard of effective nerve conduit. Therefore, how to mimic and maintain dynamic repair-supportive microenvironments that are beneficial to peripheral nerve regeneration is a priority to design bioactive NGCs.

Bioceramics have been widely used in the field of bone and soft tissue regeneration due to their key properties to maintain a repair-supportive microenvironments [19]. However, little is known on whether inorganic bioceramics can have potential for enhancing peripheral nerve regeneration and what are the mechanisms underlying their actions. Previous studies have showed that lithium (Li) element has been widely used in the central nervous system (CNS) for the treatment of trauma and chronic neurodegenerative diseases, such as Alzheimer's disease, Huntington's disease, and Parkinson's disease, due to its anti-apoptotic, anti-inflammatory and neuroprotective properties [20–22]. Actually, treatment with combination of Li chloride and polycaprolactone enhances peripheral nerve regeneration and Li ions appear to be valuable for promoting peripheral nerve regeneration [23,24]. Magnesium (Mg) ions can stimulate nerve fibers regeneration without obvious cytotoxicity [25–27]. Our prior studies have shown that Si-containing compounds can simultaneously stimulate the differentiation of multiple types of cells towards specific lineages [28–30]. In addition, recent studies have indicated that ions released by biomaterials can modulate the immune microenvironment [31–33]. Some ions, such as Mg [32], zinc (Zn) [34], molybdenum (Mo) [35], manganese (Mn) [36] and strontium (Sr) [37] can suppress the secretion of inflammatory cytokines by macrophages, thereby promote tissue regeneration. However, whether these aforementioned inorganic ions can be used to maintain the repair-supportive environments that can facilitate peripheral nerve regeneration remains to be answered.

In the current study, the Li–Mg–Si (LMS) bioceramics and LMS-containing scaffolds were generated. The LMS-containing scaffolds are found to promote the peripheral nerve regeneration by providing a dynamic immuno-modulatory and repair-supportive microenvironment. This study indicates that LMS bioceramics can be applied as a promising biomaterial for promoting peripheral nerve regeneration.

2. Materials & methods

2.1. Fabrication and characterization of Li–Mg–Si (LMS) bioceramics and LMS-containing scaffolds

The LMS powders were made of with lithium nitrate ($LiNO_3$), magnesium nitrate hexahydrate ($Mg(NO_3)_2{\cdot}6H2O$), and tetraethyl orthosilicate (Sinopharm Chemical Reagent, China) by sol-gel method [30]. The nanofibrous scaffolds containing LMS bioceramics were prepared by an electrospinning process using PCL (Mn = 80 kDa) and 1,1,1,3,3,3-hexafluoro-2-propanol (HFIP, Alladin Reagent, China). 0 g, 0.025 g, 0.05 g, 0.1 g and 0.15 g LMS bioceramics were suspended in 10 mL HFIP solution and were ultra sonicated for 30 min, followed by addition of 1 g PCL for 24 h to obtain 0, 2.5, 5, 10 or 15% LMS bioceramics respectively. This option of concentrations of LMS bioceramics was based on our prior experience that concentrations of LMS bioceramics higher than 15% led to significant cytotoxicity. The mixed solutions were next poured into a 10-mL syringe with a 20-gauge needle, followed by electrospinning at room temperature with an electric field strength of 10 kV, a 12 cm air gap distance, and a flow rate of 0.02 mL/min at 50–60% relative humidity [38–40]. The produced nanofibrous materials were dried in the air at room temperature for 48 h under a roller rotating at 200–300 rpm. The prepared scaffolds containing different amounts of LMS bioceramics (0, 2.5, 5, 10 or 15%) were named as PCL, 2.5LMS-PCL, 5LMS-PCL, 10LMS-PCL, and 15LMS-PCL, respectively. Indicated scaffolds were rolled up into a conduit using a custom mold for the *in-vivo* experiments.

The morphology of LMS bioceramics and scaffolds was examined under a scanning electron microscope (SEM, JSM-6700F, JEOL, Japan). Transmission electron microscope (TEM, F200X G2, FEI TALOS, USA) was used to determine the distribution of LMS particles in the fibers. The size distribution of the LMS bioceramic particles was detected by a laser particle size analyzer (Mastersizer 2000, Malvern, England). The powders and scaffolds were characterized by X-ray photoelectron spectroscopy (XPS, Thermo Scientific ESCALAB 250Xi, USA), and X-ray diffractometer (XRD, D8, Bruker AXS, Karlsruhe, Germany) using Cu Kα radiation and operating at 40 KV with 40 mA, as well as scanned from 10° to 90° for 2θ angles at a scanning rate of 5°/min. To evaluate ion release from the scaffolds, samples of the different scaffolds (2.5 cm × 5 cm each) were soaked in 10 mL of phosphate-buffered saline (PBS) at 37 °C in a shaker for different time periods (1, 3, 5, or 7 days) and collected longitudinally. The concentrations of Li, Mg and Si ions in the collected samples were analyzed using inductively coupled plasma optical emission spectrometer (ICP, Varian 715-ES). The pH values of the collected solutions were measured.

2.2. In vitro

2.2.1. Cell culture

Rat Schwann cells (RSC96) and murine macrophage RAW264.7 cells were from Typical Culture Preservation Commission Cell Bank, Chinese Academy of Sciences (Shanghai, China). RSC96 and RAW264.7 cells were cultured in Dulbecco's Modified Eagle Medium (DMEM, Gibco) containing 10% FBS (Cyagen Biosciences, China) and 1% penicillin/streptomycin in a 5% CO_2 incubator at 37 °C.

2.2.2. The proliferation, wound healing and differentiation of RSC96 cells

The LMS extracts were prepared, according to ISO 10993–5. The LMS particle samples (200 mg each) were suspended in 1 mL of medium, and shaken in 120 rpm at 37 °C for 24 h, followed by centrifuging at 1000 rpm for 10 min. Their supernatants were collected and filtered through a 0.22 μm filter as the LMS extract stock solution (200 mg/mL). The sock solutions were diluted using the medium as 1:2, leading to 1/2 (102.4 mg/mL), 1/4 (51.2 mg/mL), 1/8 (25.6 mg/mL), 1/16 (12.8 mg/mL), 1/32 (6.4 mg/mL), 1/64 (3.2 mg/mL), 1/128 (1.6 mg/mL), and 1/256 (0.8 mg/mL), 1/512 (0.4 mg/mL), 1/1024 (0.2 mg/mL) for subsequent biological studies. The concentrations of Li, Mg and Si ions in the

collected samples were analyzed using inductively coupled plasma optical emission spectrometer (ICP, Varian 715-ES).

RSC96 cells (2×10^3 cells/well) were cultured in 96-well plate and treated in triplicate with the different concentrations of LMS solutions for 1, 3 or 7 days. The proliferation of RSC96 cells at each time point was measured by the CCK-8 assay using the specific kit (Sigma, USA), per the manufacturer's protocol. The absorbance of the culture supernatants in individual wells was measured at 450 nm using a microplate reader (SpectraFluor Plus, Tecan, Crailsheim, Germany).

The effects of LMS extracts on the wound healing of RSC96 cells were examined by the wound healing assay. Briefly, RSC96 cells (2×10^4 cells/well) were cultured in 12-well plates overnight. The formed cell monolayers were wounded by scratching with a 200-μL pipette tip. After being washed with PBS, the wounded monolayer of cells was treated in triplicate with different concentrations of serum-free LMS extracts (1/64, 1/128 or 1/256) and the wound healing of RSC96 cells was observed at 0, 12, and 24 h post wounding by photoimaging under an inverted light microscope (Model: IX71, Olympus, Japan).

RSC96 cells (2×10^5 cells/well) were cultured in 6-well plates and treated with the different concentrations of LMS extracts for 24 h. The expression of myelination-related genes in RSCs was analyzed by RT-qPCR using specific primers in Table S1. The expression of myelination-related proteins in RSC96 cells was analyzed by immunoblotting assays. Briefly, the different groups of cells were lysed in RIPA lysis buffer (Beyotime, China) and after being centrifuged, the cell lysates were separated by SDS-PAGE on 4–20% gels (GenScript, China) and transferred onto polyvinylidene difluoride membranes. Immunoblots were generated by incubation overnight at 4 °C with primary antibodies against NGF (Abcam, ab52918, 1:1000), PMP22 (Abcam, ab270400,1:1000), NCAM (Abcam, ab220360, 1:1000) and horseradish peroxidase (HRP)-conjugated secondary antibodies. The impact of LMS extracts on the expression of S100 protein in different groups of RSC96 cells was tested by immunofluorescence using rabbit monoclonal anti-S100β antibody (1:100; cat. no. ab52642, Abcam) and DAPI (Southern Biotech, England), TSAPlus kit (G1236, Servicebio, China), following the manufacturer's instructions. The cells were scanned using a Panoramic Scanner with Pannoramic DESK, P-MIDI, P250 (3D HISTECH, Hungary).

2.2.3. The polarization of RAW264.7 cells

RAW264.7 cells (2×10^5 cells/well) were cultured in 6-well plates and treated in triplicate with the different concentrations of LMS extracts for 3 days. The cells were harvested and the impact of LMS extracts on M1/M2 polarization was analyzed by flow cytometry using antibodies against CD86 (1:50 dilution, BioLegend, USA) and CD206 (1:400, BioLegend, USA) and Dylight 488-*anti*-mouse secondary antibodies in a Flow cytometry (BD Accuri C6, USA). The relative levels of iNOS, tumor necrosis factor-alpha (TNF-α), arginase 1 (Arg-1), Cluster of Differentiation 206 (CD206) gene mRNA transcripts to the control GAPDH in the different groups of RAW264.7 cells were quantified by qRT-PCR using specific primers in Table S1. The related levels of protein expression in the different groups of RAW264.7 cells were measured by immunoblotting assays using primary anti-Arg-1 (1:1000, Abcam, ab91279), anti-iNOS (1:1000, Abcam, ab49999), and HRP-conjugated secondary antibodies.

2.2.4. Effects of LMS-containing scaffolds on the proliferation, wound healing and differentiation of RSC96 cells

The impact of different scaffolds on the viability of RSC96 cells was analyzed using the live/dead cell staining kit (Dojindo, Japan). The scaffolds were evaluated by a fluorescence microscope (DMi8 S, Leica) and a laser confocal scanning microscope (TCS SP8, Leica) at 488 nm for excitation to detect Calcein-AM stained living cells (green) and 556 nm for excitation to detect PI-stained dead cells (red). The proliferation of RSC96 cells cultured on different scaffolds for 1 or 3 days was tested by CCK-8 (Sigma, USA). The levels of myelination-related gene mRNA transcripts to the contorl GAPDH in individual groups of RSC96 cells were quantified by RT-qPCR. The expression levels of myelination-related proteins in individual groups of RSC96 cells were characterized by immunoblotting.

To analyze the transcriptome profiles, RSC96 cells were cultured on the LMS-containing or control PCL scaffolds for 1 day and their total RNA was extracted using TRIzol reagent (Invitrogen, USA), according to the manufacturer's instructions. The RNA samples were reverse-transcribed into cDNA to construct libraries using the VAHTSTM Total RNA-Seq (H/M/R) Library Prep Kit (VAHTSTM, China). The RNA libraries were sequenced and the differentially expressed genes (DEGs) were identified by TopHat and Cufflinks using the Fragments Per Kilobase of transcript per Million mapped reads (FPKM) method. The DESeq algorithm was used to screen DEGs between groups. The biological functions of the DEGs were analyzed by GO enrichment analysis (http://www.geneontology.org/).

XAV-939 (Selleck, China) was dissolved in dimethyl sulfoxide (DMSO) at a stock concentration of 10 mM, and served as a highly selective inhibitor of the Wnt/β-catenin. To evaluate the involvement of the Wnt/β-catenin signaling in the remyelination of RSC96 cells mediated by LMS, RSC96 cells were pre-treated with XAV-939 (20 μM) for 2 h and subsequently cultured with different scaffolds. The levels of myelination-related gene expression in individual groups of cells were determined by RT-qPCR and immunoblotting.

2.2.5. Single cell RNA sequencing (scRNA-seq) analysis of macrophages cultured on LMS containing scaffolds

The impact of LMS-containing scaffold on RAW264.7 cell polartiation was analyzed by single cell RNA sequencing (scRNA-seq). In Briefly, RAW264.7 cells (2×10^5 cells/well) were cutlured on the contorl PCL or LMS-containing scaffolds for 3 days and harvested, followed by preparing single cell suspension, according to the 10x Genomics® Cell Preparation Guide of the manufacture. The cell suspension was loaded into Chromium microfluidic chips with 3′ chemistry and barcoded with a 10 × Chromium Controller (10X Genomics). Total RNA was extracted from the barcoded cells and reverse-transcribed to construct libraries using a Chromium Single Cell 3′ reagent kit (10X Genomics), according to the manufacturer's instructions. The RNA libraries were sequenced in Illumina (NovaSeq), according to the manufacturer's instructions (Illumina). After quality control of raw reads performed by FastQC, the raw reads were demultiplexed and mapped to the reference genome in the 10X Genomics Cell Ranger pipeline (https://support.10xgenomics.com/single_cell_gene_expression/software/pipelines/latest/what_is_cell_ranger) using default parameters. The quality of all 20661 spots was controlled (Table S2). The scRNA expression matrices were analyzed using the 'Seurat' package v4.1.1 in R v4.1.0. All samples were combined using the 'FindIntegrationAnchors' function. Dimensionality reduction and clustering were performed by principal component analysis (PCA) using the 'RunPCA' function. The DEGs were analyzed by the 'FindAllMarkers' function. The potential functions of these DEGs were analyzed by functional enrichment analysis, including GO and KEGG using the 'clusterProfiler' package. Transformation of scRNA-seq counted data was performed by scSTAR [41]. The global transcriptomic profiles were analyzed by Trajectory analysis using the monocle3 package. All data were visualized using the 'ggplot2' and 'ggsci' packages.

2.2.6. Effects of polarized macrophages by LMS containing scaffold on SC proliferation, migration and myelination in vitro

To explore the effect of LMS-containing scaffolds on macrophage polarization, RAW264.7 cells (2×10^5 cells/well) were cultured on the contorl PCL or 5LMS-PCL scaffolds in the presence or absence of 1 μg/mL of lipopolysaccharide (LPS, Sigma, USA) for 72 h. Similarly, RAW264.7 cells were treated with, or without (the contorl), LPS in DMEM for 72 h. The cells were isolated and subjected to immunofluorescent staining and flow cytometry using the primary antibodies against CD68, CD206 and

iNOS (Abcam, USA), and secondary antibody Alexa Fluor 488 goat anti-mouse IgG (1:200, Abacam, USA) and Alexa Fluor 594 goat anti-rabbit IgG (1:200, Abcam, USA) as well as nuclear staining with DAPI.

The relative leves of interleukin-1α (IL-1a), interleukin-1β (IL-1β), IL-6, IL-10, TNF-α, iNOS mRNA transcripts to the contorl GAPDH in individual groups of RAW264.7 cells were quantified by qRT-PCR. The expression levels of inflammatory proteins in those RAW264.7 cells were measured by immunoblotting using primary antibodies anti-Arg-1 (1:1000, Abcam, ab91279) and anti-iNOS (1:1000, Abcam, ab49999), and HRP-conjugated secondary antibodies.

The influence of polarized macrophages on the proliferation, wound healing and myelination of RSC96 cells was examined. Briefly, RAW264.7 cells were cultured on the PCL or 5LMS - PCL scaffolds for 3 days and their suppernatants were harvested as stimulati. RSC96 cells were cultured in the medium supplemented with the stimulati at a ratio of 1:1. The proliferation and wound healing of RSC96 cells were determined by the CCK-8, wound healing and transwell migration assays, respectively. The levels of myelination-related gene mRNA transcripts to the contorl GAPDH in individual groups of RSC96 cells were quantified by RT-qPCR.

2.3. In vivo

The animal experiment protocols were approved by the Animal Experiment Ethics Committee of Shanghai Ninth People's Hospital affiliated to Shanghai Jiao tong University, China. The studies were designed according to the guidelines of the Animal Research: Reporting of *In Vivo* Experiments (ARRIVE).

2.3.1. Animal surgery

Sprague–Dawley (SD) rats (male, weighing 280–320 g) were obtained from the Experimental Animal Centre of the Ninth People's Hospital and housed in a specific pathogen-free facility with controlled temperature 22 ± 2 °C; humidity 55 ± 5%; a light/dark cycle of 12/12 h, free access to water and food. To induce sciatic nerve injury, the rats were anesthetized with isoflurane gas and subjected to a skin incision for the exposure of their left sciatic nerve, followed by creating a 10-mm segmental defect. The average size of the LMS-containing conduct used in animal studies is 12 mm (length)/2 mm (inner diamter)/0.5 mm (thickness). The wound proximal and distal nerve stumps were fixed with the control PCL NGC or 5LMS-PCL using 8–0 nylon sutures. In the autograft group, a 10 mm nerve segment was resected, reversed 180° and sutured. The wound was subsequently closed. All rats were housed and fed routinely until being euthanized at the designated time points.

2.3.2. Walking track analysis

The functional recovery of individual rats was assessed by walking track analysis at 12 weeks post-operation. Briefly, individual rats were tested in a confined walkway (10 cm × 100 cm long covered with white paper), and their ink footprints were recorded for the analysis of the sciatic functional index (SFI) as described previously [14,42]. An SFI of 0 is considered as normal function, and an SFI of −100 represents complete loss of function.

2.3.3. Electrophysiology

The functional recovery of the regenerated nerve in individual rats was examined by electrophysiology. In brief, individual rats were anesthetized and their left sciatic nerve was re-exposed and isolated. the proximal end of the sciatic nerve trunk of each rat was placed with bipolar stimulating electrodes. The time to deflection (latency) and compound muscle action potentials (CMAPs) on the gastrocnemius belly was recorded using an 8-channel physiologic signal recorder (RM-6280C, Chengdu Instrument Factory, China).

2.3.4. Evaluation of gastrocnemius muscle

Both experimental and control sides gastrocnemius muscles were dissected from individual rats and weighed. The muscle moist weight ratio was calculated as: the moist weight of the experimental side muscle divided by the weight of the control side × 100%. The muscles were fixed and paraffin-embedded and their sections were routine-stained with hematoxylin and eosin (H&E) and Masson staining.

2.3.5. Histologic, morphologic, immunohistochemical and immunofluorescent evaluation of regenerated nerves

Individual animals were euthanized at 4 or 12 weeks post injury and their left nerve was dissected. The nerve samples were prepared for transmission electron microscopy (TEM). Briefly, the nerve samples were fixed with 2.5% glutaraldehyde (Solarbio, China), subjected to ultrathin sections (70 nm), and stained with lead citrate and uranyl acetate, followed by observing and photoimaging in a TEM (HITACHI, HT7700 Exalens, Japan). Some nerve samples were fixed with 10% buffered formalin, and embedded in paraffin. The middle portion of the nerve conduits in individual rats was sectioned at 3 mm in thickness and stained with H&E, Toluidine Blue (Solarbio, China) and immunohistochemistry using anti-CD31 (Proteintech, 11265-1-AP, China) for examination under a light microscopy (Leica, DM3000, Germany).

Some nerve sections were analyzed by immunofluorescence using the TSAPlus kit (G1236, Servicebio, China) per the manufacturer's instructions. Briefly, the sections were subjected to antigen retrieval and treated with a tissue spontaneous fluorescence quencher (G1221, Servicebio). Subsequently, the sections were stained with primary antibodies of anti-S100 β (1:100, Abcam, ab52642), anti-neurofilament 200 (NF200, 1:150, Proteintech, 60331-1-Ig, China), anti-PMP22 (1:1000, Abcam, ab270400), anti-NCAM (1:1000, Abcam, ab220360), anti-PGP9.5 (1:1000, Abcam, ab10404), anti-β-catenin (1:1000, Cell Signaling Technology, #8480), anti-CD68 (1:100, Abcam, ab31630), anti-Mannose Receptor (1:100, Abcam, ab64693), anti-iNOS (1:70, Abcam, ab15323), and the secondary antibodies of goat anti-mouse IgG (1:200, Sigma, USA) and goat anti-rabbit IgG (1:200, Sigma, USA) as well as DAPI (1:200, Life Technologies, USA) for staining of cell nuclei. All sections were scanned using a Panoramic Scanner with Pannoramic DESK, P-MIDI, P250 (3D HISTECH, Hungary), and fluorescence intensity values were measured using the ImageJ software (National Institutes of Health, USA).

2.4. Statistical analyses

All statistical analyses were performed using GraphPad Prism 8.0 (GraphPad Software, USA). Quantitative data were obtained from at least three independent experiments and are presented as mean ± standard deviation (SD). Comparisons between groups and among groups were performed by an unpaired student's t-test and one-way ANOVA and Tukey's method, respectively. The statistical significance was set when a p-value of <0.05.

3. Results

3.1. Characterization of LMS bioceramic particles

Following the preparation of LMS bioceramic particles and LMS-containing scaffolds using poly (ε-caprolactone) (PCL) as a matrix, the morphology of LMS bioceramic particles was characterized by scanning electron microscopy (SEM). The images displayed that the particles were amorphous and agglomerated (Fig. 1A). The average diameter of LMS particles was 2.477 μm (d0.5 = 2.477 μm) (Fig. S1A). Energy-dispersive spectroscopy (EDS) mapping clearly exhibited the uniform distributions of Mg and Si elements (Fig. 1A). X-ray diffraction (XRD) revealed that the major phase of the LMS bioceramics was Li_2MgSiO_4 (Fig. 1B). Elemental composition analysis by X-ray photoelectron spectroscopy (XPS) identified the presence of Li^+, Mg^{2+}, and Si^{4+}, based on a peak at approximately 54.0 eV, 1302.0 eV, and 101.0 eV in the Li1s, Mg1s and Si2p spectra, respectively (Fig. 1C).

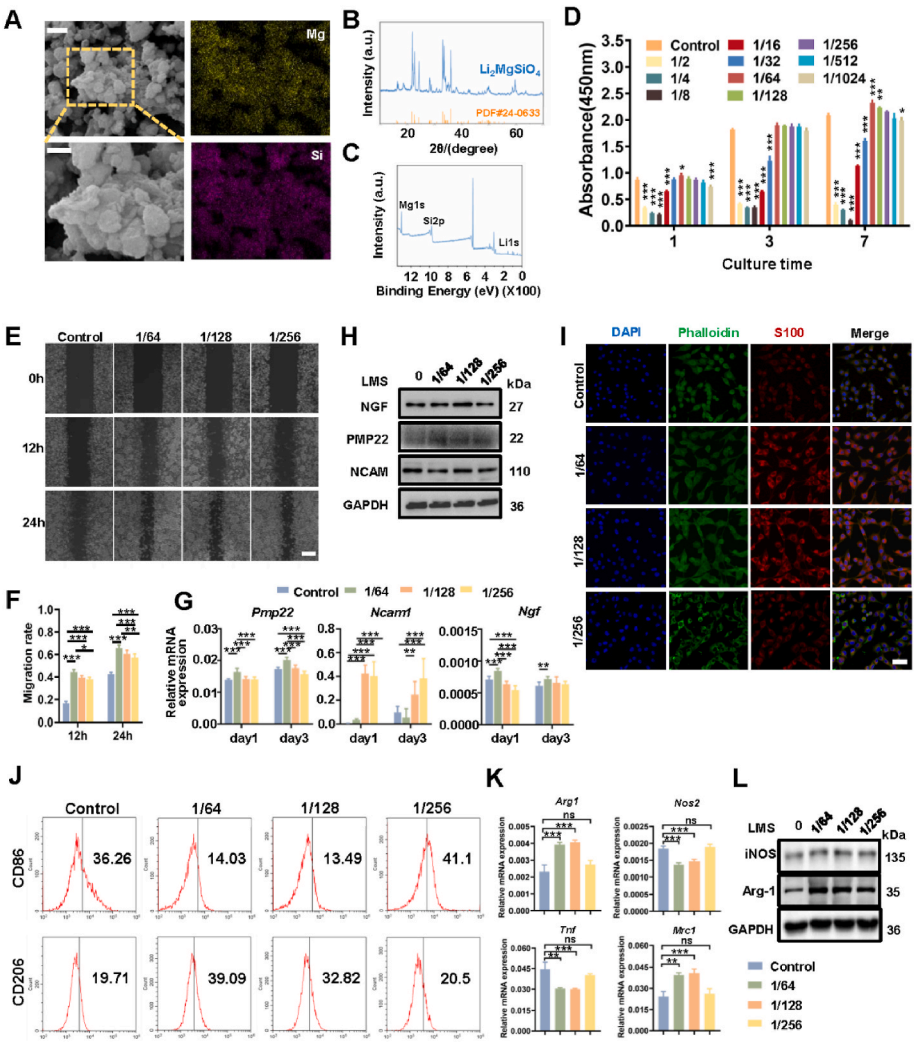

Fig. 1. LMS bioceramic extracts promote the proliferation, migration and differentiation of RSCs, and regulate the polarization of macrophages in vitro.
(A) Electron microscopy scanning displayed that the LMS bioceramics are amorphous and agglomerated, and the EDS mapping indicated the uniform distribution of Mg and Si ions. Scale bars = 2 and 1 μm.
(B) XRD pattern of LMS bioceramics exhibited that the major phase was Li_2MgSiO_4.
(C) XPS analysis of the chemical elemental composition of LMS bioceramics.
(D) The effects of different concentrations of LMS extracts on the viability of RSCs in the indicated time periods.
(E&F) Treatment with the indicated concentrations of LMS extracts promoted the wound healing of RSCs. Scale bars = 200 μm.
(G) RT-qPCR analysis of the relative levels of myelination-related gene mRNA transcripts in RSC96 cells after treatment with vehicle or LMS extracts at different dilutions (1/64, 1/128 and 1/256) for the indicated time periods.
(H) Western blot analysis of the relative levels of myelination-related protein expression in RSC96 cells after treatment with vehicle or LMS extracts at different dilutions (1/64, 1/128 and 1/256) for 24 h.
(I) Representative immunofluorescent images of RSCs that had been treated with vehicle or LMS extracts at different dilutions (1/64, 1/128 and 1/256) for 24 h. The cells were stained with phalloidin (green), nuclei (blue) and anti-S100 (red). Scale bars = 100 μm
(J) Flow cytometry analysis of RAW264.7 cells that had been treated with vehicle or LMS extracts at different dilutions (1/64, 1/128 and 1/256) for 3 days. (K) RT-qPCR analysis of the relative levels of macrophage polarization-related gene mRNA transcripts in RAW264.7 cells after treatment with vehicle or LMS extracts at different dilutions (1/64, 1/128 and 1/256) for 3 days.
(L) Western blot analysis of the relative levels of macrophage polarization-related protein expression in RAW264.7 cells after treatment with vehicle or LMS extracts at different dilutions (1/64, 1/128 and 1/256) for 3 days.

3.2. *LMS extracts have pro-myelination functions in vitro*

Next, the potential toxicity and function of LMS extracts were tested in rat Schwann RSC96 cells. The concentrations of Li ion in LMS extracts (1/256, 1/128, 1/64) were 84.79 mg/L, 165.19 mg/L and 341.01 mg/L, respectively. The concentrations of Mg ion were 106.17 mg/L, 207.21 mg/L, 409.74 mg/L respectively and those of Si ion were 175.35 mg/L, 357.34 mg/L and 753.98 mg/L respectively (Fig. S1B). The CCK-8 assay indicated that treatment with LMS extract solutions at higher concentrations (<1:64 dilutions), but not with a lower concentration (>1:64 dilutions), significantly reduced the viability and inhibited the proliferation of RSC96 cells, which could reflect the high alkalinity-induced cytotoxicity to RSC96 cells (Fig. 1D). Interestingly, treatment with LMS extract solutions at low or moderate concentrations (1:64 or 1:128 dilutions), significantly increased the proliferation of RSC96 cells (Fig. 1D). The wound healing assay displayed that treatment with LMS extract solutions at lower concentrations (1:64–1:256 dilutions) significantly promoted the migration activity of RSC96 cells (Fig. 1E&F), a function critical in the bridging of injured gap at the early stage of nerve repair and regeneration [43]. Accordingly, we hypothesized that LMS nanoparticle exposure might modulate the myelination of RSC96 cells. Real time quantitative polymerase chain reaction (RT-qPCR) analysis indicated that treatment with the LMS extract solution at 1:64 dilution significantly increased the relative expression levels of peripheral myeline protein 22 (*Pmp22*) and nerve growth factor (*Ngf*) gene transcripts, while treatment with a lower concentration of LMS solution had a reduced effect, even decreased their transcripts in RSC96 cells (Fig. 1G). However, treatment with the LMS solutions at 1:128 or 1:256 dilution, but not at 1:64 dilution, significantly up-regulated the expression of the neural cell adhesion molecule 1 (*Ncam1*) gene in RSC96 cells (Fig. 1G). Such changes in the transcription of those genes are associated with a switching from an un-myelinated to myelinated status in SCs [17]. Similar results of the relative expression levels of those proteins were observed by immunoblotting in RSC96 cells (Fig. 1H). Further immunofluorescent staining revealed that cytoskeletal re-organization occurred in the polypod morphology of RSC96 cells (Fig. 1I), indicating that exposure to LMS extracts induced a differentiation of RSC96 cells [44]. Together, these results indicated that the LMS nanoparticle extracts supported the myelination of SCs in vitro.

3.3. *LMS extracts modulate the polarization of RAW264.7 cells in vitro*

To evaluate the effect of LMS bioceramic particles on macrophage activation and polarization, RAW264.7 cells were cultured with LMS extracts at the indicated dilutions (1/64, 1/128, 1/256) for 3 days. CD86, iNOS, and TNF-α were regarded as biomarkers of M1 macrophage, while CD206 and Arg-1 were regarded as M2 macrophage markers. Flow cytometry analysis exhibited that LMS extract treatment

at 1:64 or 1:128 dilutions decreased the levels of CD86 expression, but increased CD206 expression in RAW264.7 cells (Fig. 1J). Similarly, RT-qPCR unveiled that the same treatment also decreased the relative levels of iNOS and TNF-α mRNA transcripts, but increased Arg-1 and CD206 mRNA transcripts in RAW264.7 cells, compared with that in the untreated controls (Fig. 1K). Western blotting analysis exhibited similar trends in the expression levels of Arg-1 and iNOS proteins in the different groups of RAW264.7 cells (Fig. 1L). Therefore, the ions in the LMS extract solutions at the appropriate dilutions (1:64 and 1:128) effectively promoted M2 polarization to modulate the immune microenvironment.

3.4. LMS-containing scaffolds enhances the pro-myelination functions of RSC96 cells dependent on the β-catenin signaling

Scaffolds containing different amounts of LMS bioceramics (0, 2.5, 5, 10 and 15%) were labeled as PCL, 2.5LMS-PCL, 5LMS-PCL, 10LMS-PCL, and 15LMS-PCL, respectively. The topography of the scaffolds was observed by SEM (Fig. 2A) and TEM (Fig. S2A). The average fiber diameters of PCL, 2.5LMS-PCL, 5LMS-PCL, 10LMS-PCL, and 15LMS-PCL fibers were 437.98 ± 139.17, 445.62 ± 140.51, 483.98 ± 143.73, 492.89 ± 146.84, 493.73 ± 102.55, respectively (Fig. S2B). The XRD spectra for all of the scaffolds containing LMS bioceramics exhibited diffraction peaks at approximately 21.2° and 23.5°, closely matching the spectrum for PCL, indicating that incorporation of LMS bioceramics did not affect the chemical construction of PCL (Fig. S3). As expected, there was no obvious peak representing Li_2MgSiO_4, likely due to the low concentrations of LMS bioceramics in each preparation. As shown in Figs. S4A–C, the concentrations of Li, Mg and Si ions released from the LMS-containing scaffolds into PBS increased, paralleling with the increased concentrations of LMS bioceramics in the PCL membranes. Notably, the concentrations of Li and Si ions in the surrounding solution slowly increased over time and reached a plateau, while the concentration of Mg ion increased within the first 3 days and then decreased slightly. There was no any of the ions in the control PCL scaffold (Figs. S4A–C). Hence, the LMS-containing scaffolds effectively released

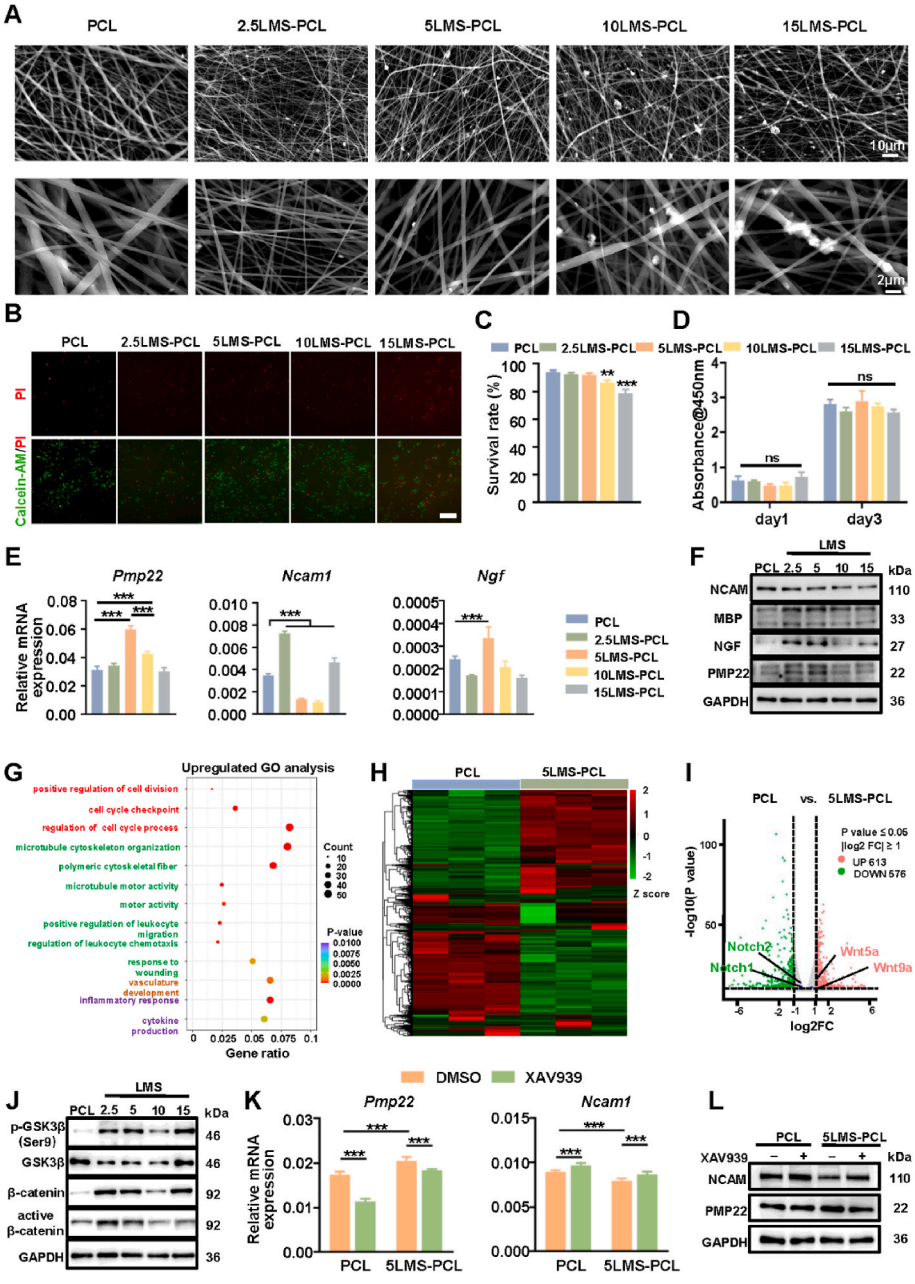

Fig. 2. LMS-containing scaffolds modulate the proliferation, migration and differentiation of RSC96 cells.
(A) SEM images of scaffolds containing different concentrations of LMS.
(B–C) Representative images and quantitative results of live-dead staining of RSC96 cells after cultured on scaffolds containing different concentrations of LMS. Scale bars = 200 μm.
(D) The effects of scaffolds containing different concentrations of LMS on the viability of RSCs.
(E) RT-qPCR analysis of the relative levels of myelination-related gene mRNA transcripts in RSC96 cells that had been cultured on scaffolds containing different concentrations of LMS for 24 h.
(F) Immunoblotting analysis of the relative levels of myelination-related protein expression in RSC96 cells that had been cultured on scaffolds containing different concentrations of LMS for 24 h.
(G) GO analysis of the enrichment of differentially expressed genes between RSC96 cells cultured on PCL and 5LMS-PCL scaffold for 24 h followed by RNA sequencing.
(H–I) Differentially expressed genes between RSC96 cells cultured on PCL and 5LMS-PCL scaffold for 24 h (|log2FC|>1 and FDR<0.05).
(J) Immunoblotting analysis of the relative protein levels of the GSK3β/β-catenin pathway in RSC96 cells cultured on scaffolds containing different concentrations of LMS for 24 h. (K) RT-qPCR analysis of the relative levels of gene mRNA transcripts in the GSK3β/β-catenin pathway in RSCs cultured on scaffolds containing different concentrations of LMS for 24 h in the presence or absence of XAV939.
(L) Immunoblotting analysis of the relative protein levels in the GSK3β/β-catenin pathway in RSC96 cells cultured on scaffolds containing different concentrations of LMS for 24 h in the presence or absence of XAV939.

bioactive ions, similar to LMS bioceramics, without affecting the chemical structure of the PCL scaffold. The pH value of the solution containing only PCL scaffold remained stable at 7.34 ± 0.05, but the pH values of the LMS-containing scaffolds slightly increased, according to the concentrations of LMS bioceramics, suggesting that the LMS bioceramics might contribute to the formation of an alkaline environment (Fig. S4D).

The effects of LMS-containing scaffolds on the proliferation and differentiation of RSC96 cells were further evaluated. The results from the live/dead staining and CCK-8 assays revealed that the LMS-containing scaffolds had no obvious cytotoxicity against RSC96 cells (Fig. 2B–D). Furthermore, RT-qPCR and immunoblotting analyses unveiled that exposure to the LMS-containing scaffolds, especially those containing 5% LMS bioceramic particles (5LMS-PCL), led to a significant increase in both the levels of PMP22, myelin basic protein (MBP) and NGF transcripts and protein expression, but a decrease in the levels of NCAM expression in RSC96 cells (Fig. 2E&F). These results indicated that the LMS-containing scaffolds supported the myelination of SCs, similar to those of the LMS particle extracts.

To gain functional and mechanistic insight into the effects of the LMS bioceramics on SCs, we compared the transcriptomes of RSC96 cells cultured on PCL or 5LMS-PCL. Compared with the cells on PCL, there were 864 differentially expressed genes (DEGs) in the RSC96 on 5LMS-PCL (|log2fold change|>1, false discovery rate [FDR]<0.05), of which, 634 genes were upregulated and 576 were downregulated. Gene Ontology (GO) enrichment analysis revealed that several DEGs were enriched and they are involved in several critical functions of SCs during the process of nerve regeneration, including cell proliferation, cell migration, and angiogenesis (Fig. 2G).

Additionally, the analysis revealed that several genes involved in the WNT/β-catenin and Notch pathways were affected by LMS (Fig. 2H&I). Both the β-catenin and Notch pathways are crucial for the differentiation of many types of cells, including SCs [44]. The transcriptomes of RSC96 cells exposed to 5LMS-PCL tended to enhance the WNT/β-catenin pathway and attenuate the Notch pathway (Fig. 2I). Evidently, exposure to the LMS-containing scaffold significantly increased the relative levels of glycogen synthase kinase 3 beta (GSK3β) at Ser9 phosphorylation in RSC96 cells (Fig. 2J), a well-known phosphorylation site for diminishing the inhibitory function of GSK3β in β-catenin [45]. Conversely, treatment with LMS-containing scaffolds significantly up-regulated total and

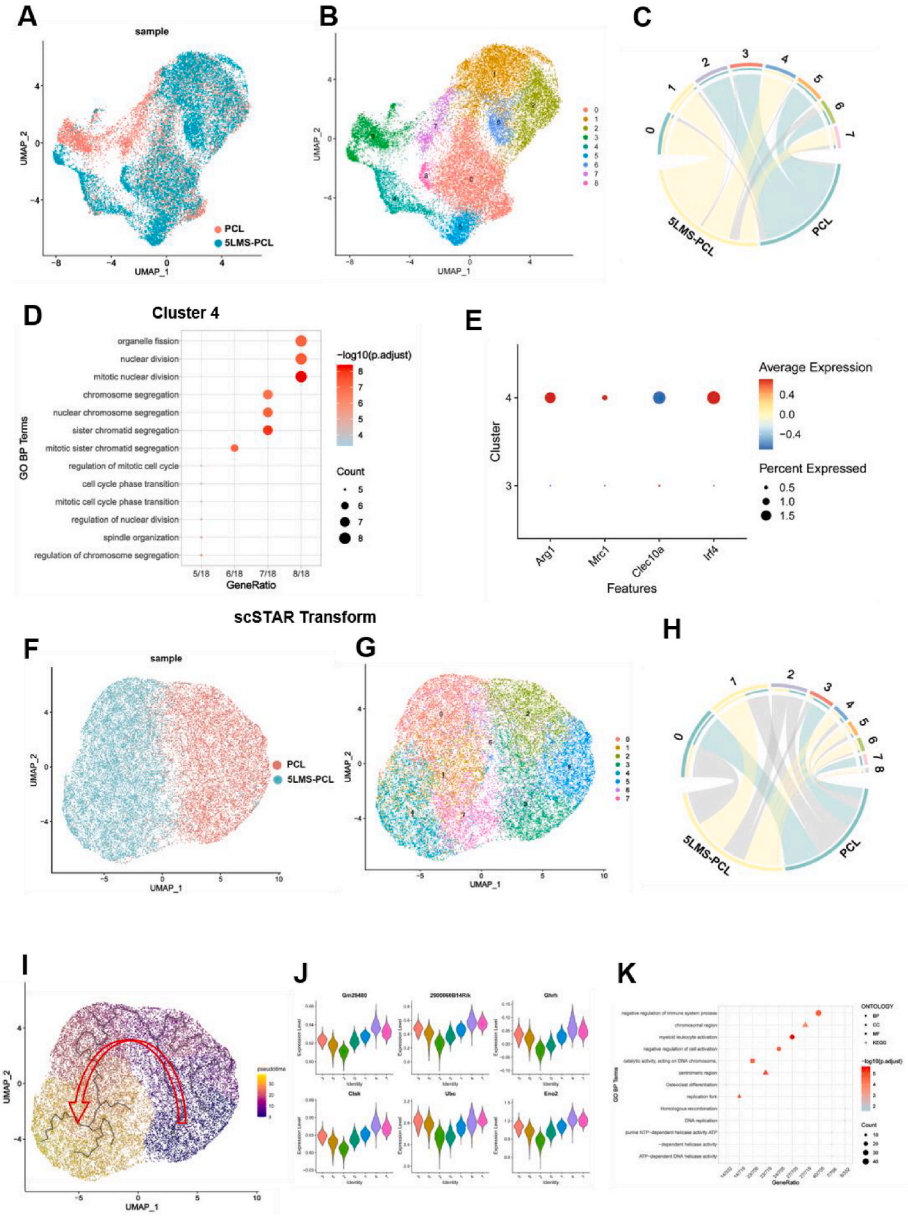

Fig. 3. Single cell RNA-seq analysis of macrophages polarized by LMS-containing scaffold
(A) UMAP visualization of the distributions of RAW264.7 cells on different scaffolds.
(B) Identification of the 9 subclusters of cell population.
(C) Hypergeometric distribution analysis of the groups (PCL or 5LMS-PCL) of each cell clusters.
(D) Gene ontology (GO) functional enrichment analysis.
(E) Visualization of the selected marker genes of M2 macrophage.
(F) UMAP visualization of RAW264.7 cells on different scaffolds after the scSTAR transformation
(G) Identification of the 8 subclusters of cell population after the scSTAR transformation
(H) hypergeometric distribution analysis of the groups (PCL or 5LMS-PCL) of each cell clusters after the scSTAR transformation.
(I) Pseudotime-trajectory analysis of RAW264.7 cells.
(J) Violin plot displayed the expression levels of genes along the trajectory with the p value < 0.001 (K) GO functional enrichment analysis of trajectory genes.

active β-catenin expression in RSC96 cells, relative to that in the untreated controls, indicating that LMS-containing scaffolds enhanced the activation of the WNT/β-catenin signaling (Fig. 2J). Further RT-qPCR and immunoblot assays unveiled that addition of XAC939, a widely used β-catenin inhibitor, antagonized the effect of LMS-containing scaffold on upregulating Pmp22 (PMP22) and downregulating Ncam1 (NCAM) expression in RSC96 cells (Fig. 2K&L), suggesting that the increased pro-myelination function of LMS-containing scaffolds may be dependent on enhanced activation of the β-catenin signaling in RSC96 cells.

3.5. LMS-containing scaffolds promote macrophage polarization toward M2-like cells

Following culturing RAW264.7 cells on 5LMS-PCL or control PCL scaffolds for 3 days, the cell population was characterized by scRNA-seq. After cell quality control, there were 22,719 cells of each sample for subsequent analysis. Uniform manifold approximation and projection (UMAP) indicated that the characteristics of these two populations of cells were partially overlapped (Fig. 3A). All cells were divided into nine clusters by unsupervised clustering. According to the dimensionality reduction results, features of cells in the cluster 3 and 4 were different from the rest of the cell clusters (Fig. 3B). The hypergeometric distribution analysis distinguished the distribution of the PCL or 5LMS-PCL group of cells in each cell cluster. The cluster 3 mainly contained cells on PCL scaffolds while the cluster 4 covered cells on 5LMS-PCL scaffolds (Fig. 3C). GO functional enrichment analysis predicted that the function was mainly enriched in "organelle fission", "nuclear division" and "mitotic nuclear division" (Fig. 3D). By comparing the marker genes of M2 macrophages, we found that the function of cluster 4 contained more M2 macrophages than the cluster 3, suggesting that cells had a tendency to obtain immunosuppressive function following culture on the LMS containing scaffold (Fig. 3E). However, the GO results of cluster 4 did not suggest that the function of this cell type was related to immunosuppression. To further explore why macrophages exhibited the change toward immunosuppression direction after culture on LMS containing scaffold, we used the scSTAR algorithm, which characterized each cell by dynamic features, instead of static features, so that the trivial but significant gene expression perturbations caused by treatment were amplified, and the interference problem of random heterogeneity among cells was fundamentally solved. After the scSTAR transformation, all the cells were clearly separated (Fig. 3F), and all the cells were divided into 8 clusters by unsupervised clustering (Fig. 3G). The state of each cluster was also clarified by hypergeometric distribution test (Fig. 3H). The pseudotime trajectory analysis can simulate the differentiation trajectory and changes in cells, based the gene status. We

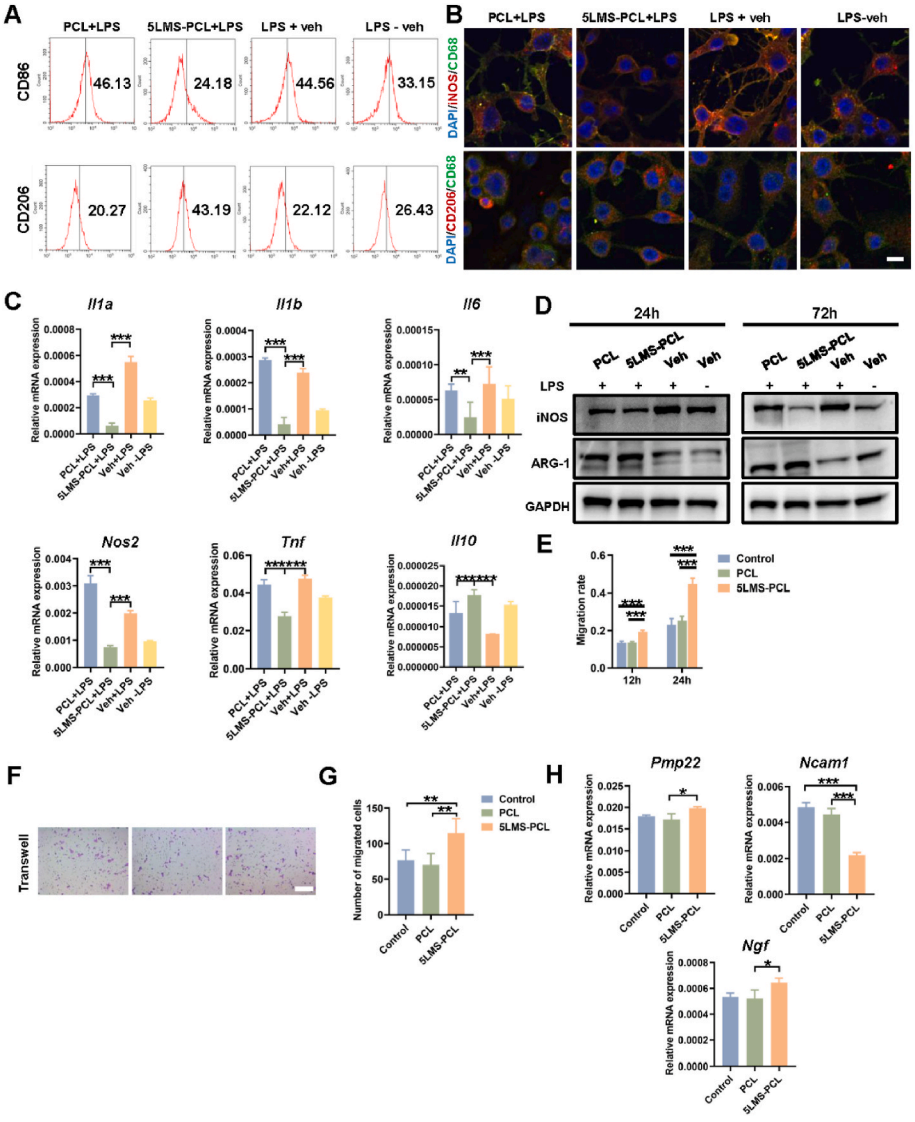

Fig. 4. Effects of polarized macrophages induced by LMS-containing scaffolds on RSC96 cell behavior.
(A) Flow cytometry analysis of RAW264.7 cells cultured on PCL or 5LMS-PCL scaffold for 24 h after LPS stimulation.
(B) Representative immunofluorescent images of different groups of RAW264.7 cells characterized by immunofluorescence staining using anti-CD68 (green), anti-iNOS (red) and anti-CD206 (red) as well as DAPI (blue). Scale bars = 150 μm
(C) RT-qPCR analysis of the relative levels of inflammation-related gene mRNA transcripts in different groups of RAW264.7 cells.
(D) Immunoblotting analysis of the relative levels of inflammation-related protein expression in different groups of RAW264.7 cells.
(E) Quantitative analysis of the wound healing capacities of RSC96 cells after coculture with different CM for the indicated time periods.
(F&G) Representative images of transwell migration and quantitative analysis of migrated RSC96 cells after coculture with different conditioned medium for 1 day. Scale bars = 200 μm
(H) RT-qPCR analysis of the relative levels of myelination-related gene mRNA transcripts in RSC96 cells after coculture with different conditioned medium for 3 days.

therefor performed pseudotime-trajectory analysis and mapped real time on the trajectory (Fig. 3I). Genes along the trajectory with a p-value of less than 0.001 were selected for functional enrichment analysis (Fig. 3J and Table S2), and the main functions of these trajectory genes were enriched in the "negative regulation of immune system process" (Fig. 3K), reflecting a feature of M2-like macrophages. Collectively, these data indicated that the LMS containing scaffolds promoted macrophages into an M2-like immunosuppression state.

3.6. LMS-containing scaffolds promote macrophage polarization to enhance the migration and myelination of RSC96 cells in vitro

Flow cytometry analysis revealed that treatment with 5LMS-PCL scaffolds decreased CD86 expression, but increased CD206 expression in RAW264.7 cells (Fig. 4A). While treatment with PCL scaffolds up-regulated iNOS expression treatment with 5LMS-PCL scaffolds enhanced CD206 expression in RAW264.7 cells (Fig. 4B). RT-qPCR analysis revealed that treatment with 5LMS-PCL scaffolds decreased the levels of IL-1α, IL-1β, IL-6, iNOS and TNF-α mRNA transcripts, but increased IL-10 transcripts in RAW264.7 cells, compared with that in the controls (Fig. 4C). Similar patterns of the levels of Arg-1 and iNOS protein expression were detected in the RAW264.7 cells cultured on 5LMS-PCL and PCL scaffolds, respectively (Fig. 4D). Thus, 5LMS-PCL scaffolds induced macrophage polarization toward the M2 phenotype.

To further investigate whether polarized macrophages could modulate the proliferation, migration and myelination of SCs, RAW264.7 cells were cultured on 5LMS-PCL scaffolds for 3 days, and their supernatants were collected as the conditional media for culture of RSC96 cells. Firstly, treatment with the conditional media failed to significantly alter the viability of RSC96 cells (Fig. S5), but promoted the wound healing and migration of RSC96 cells (Fig. 4E–G). Further RT-qPCR revealed that treatment with the conditional media significantly increased the levels of PMP22 and NGF transcripts, but decreased NCAM in RSC96 cells (Fig. 4H). Therefore, these data suggest that 5LMS-PCL scaffolds may promote macrophage polarization towards M2 to enhance the migration and myelination of RSC96 cells.

3.7. Implantation with LMS-containing NGCs promotes M2-like activation, function recovery, nerve regeneration and myelination in rats

The effect of LMS-containing NGCs on the recruitment and polarization of macrophages and subsequent influence on nerve regeneration was evaluated in a rat model of nerve injury at 1- and 2-week post-operation (Fig. 5A). Compared to PCL group, the number of SCs and $CD68^+$ macrophages notably increased in the regenerated nerve of the 5LMS-PCL group of rats at 1 and 2-week post-surgery (Fig. 5B&C). Immunofluorescent analysis displayed that the ratios of CD68+CD206+ M2-like cells to CD68+iNOS + M1 cells in the 5LMS-PCL conduit-treated rats were significantly higher than that in the PCL conduit-treated rats in both 1 and 2-week post-surgery (Fig. 5D&E). The results indicated that LMS in the NGCs effectively promoted M2-like macrophage maturation in the lesions of rats.

To explore the effectiveness of the LMS-containing NGC for supporting nerve repair *in vivo*, we employed a rat sciatic nerve defect model, in which, a 10-mm nerve gap was excised from the right sciatic nerve in Sprague–Dawley rats and bridged with PCL or 5LMS-PCL NGCs. As shown in Fig. 6A, there was no obvious inflammation, swelling and neurofibroma in all rats at 4- and 12-weeks post-surgery. Sciatic motor function analysis indicated that all groups of rats had a low value of sciatic functional index (SFI) at 4 weeks post-surgery and the SFI values gradually improved at later time points (Fig. 6B&C). More importantly, the SFI values in the 5LMS-PCL group of rats were slightly higher than

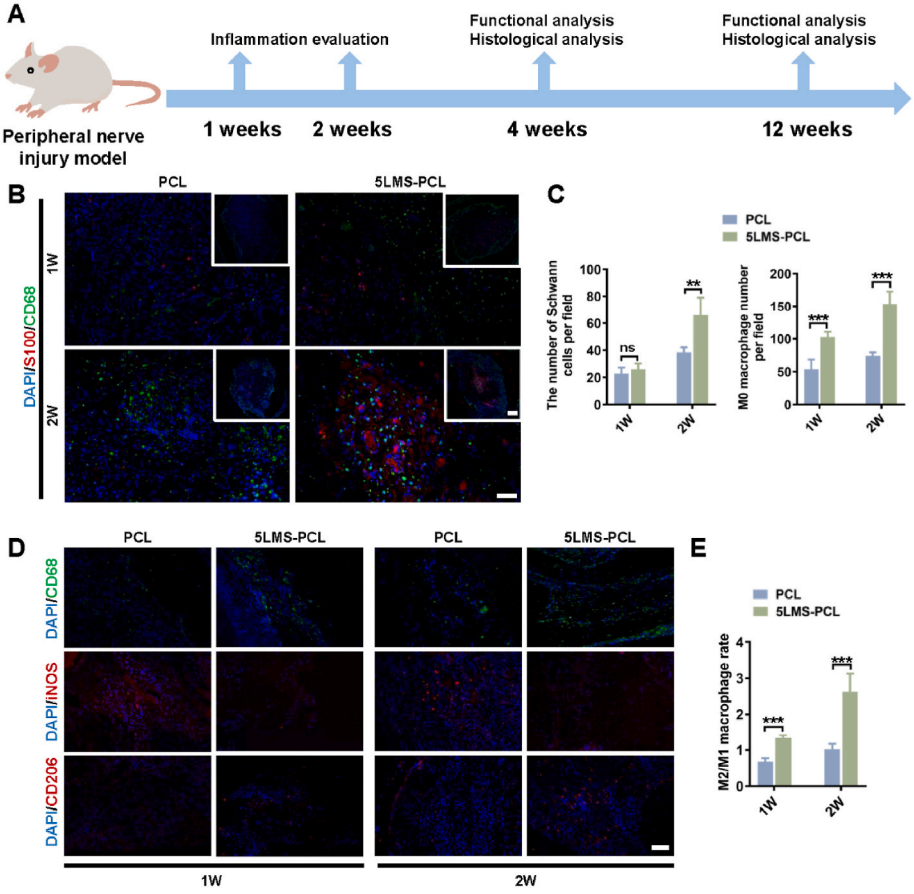

Fig. 5. Relevance between macrophages and SCs at 1 and 2 weeks after grafting of NGCs *in vivo*.
(A) A schematic illustration of *in vivo* analysis in a rat model of sciatic nerve defect.
(B) Double immunofluorescent staining of the transverse sections of grafted NGCs revealed the distribution of macrophages (M0, CD68, green) and SCs (S100, red) within different NGCs. Scale bars = 100 and 50 μm
(C) Quantitative analysis of the number of infiltrated macrophages and SCs in each group.
(D) Immunofluorescent analysis of macrophage polarization within the grafted NGCs using anti-CD68 (green), anti-iNOS (red) and anti-CD206 (red) as well as DAPI.
(E) Quantitative analysis of the ratios of $CD68^+$/$CD206^+$ macrophages to $CD68^+$/$iNOS^+$ macrophages in each group.

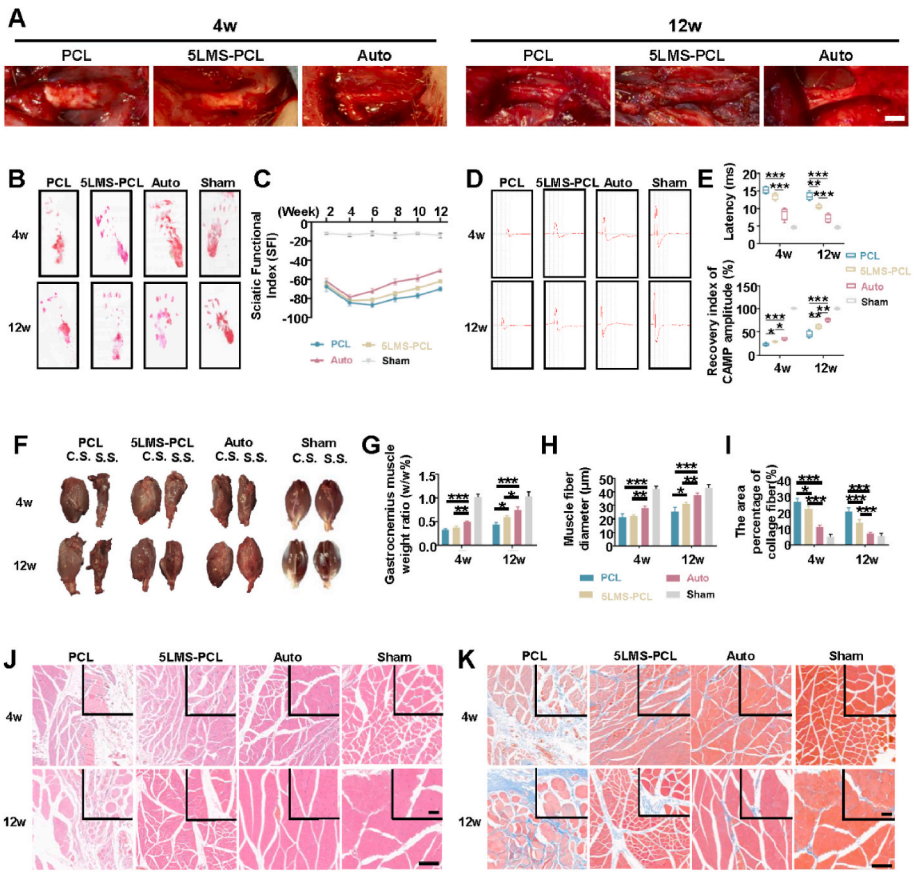

Fig. 6. LMS-containing NGCs promote motor function recovery *in vivo*.
(A) Gross observation of regenerated nerves in each group at indicated post-surgery time points. Scale bars = 5 μm
(B) Representative images of rat footprints in each group.
(C) Quantitative analysis of sciatic functional index (SFI).
(D) Representative patterns of CMAP in each group.
(E) Quantitative analysis of nerve conduction latency and CMAP amplitudes.
(F) Gross observation of gastrocnemius muscles on the surgery side (ES) and contralateral side (NS) in each group.
(G) Quantitative analysis of the wet weight ratio of gastrocnemius muscles (ES/NS).
(H–I) Quantitative analysis of gastrocnemius muscle fiber diameter and the percentage area of collagen deposition.
(J–K) Representative images of H&E staining and Masson trichrome staining of gastrocnemius muscle in each group. Scale bars = 50 and 200 μm.

that in the PCL-group throughout the observation period although they remained lower than that in the autograft control group. Electrophysiological analysis exhibited that the conduction latency in the gastrocnemius muscles of the 5LMS-PCL group was significantly shorter than that in the PCL group, but still longer than those in the autograft and sham surgery groups (Fig. 6D&E). Interestingly, the compound muscle action potential (CMAP) amplitudes in both the 5LMS-PCL and autograft groups were comparable, and significantly higher than that in the PCL group (Fig. 6E). Thus, implantation with the 5LMS-PCL NGCs promoted the recovery of motor function in rats following sciatic nerve defect.

Sciatic nerve regeneration can mitigate the nerve injury-induced atrophy of the gastrocnemius muscle. Compared with that in the controls, the ratios of the right gastrocnemius muscle weights to the control left side weights in the 5LMS-PCL group of rats were similar to that in the PCL group at 4 weeks post-surgery, but significantly higher than that in the PCL group at 12 weeks post-surgery although they in both the 5LMS-PCL and PCL groups were significantly lower than those in the autograft and sham groups at both testing time points (Fig. 6F&G). Hematoxylin and eosin (H&E) staining displayed that the fiber diameter of right gastrocnemius muscles of rats in the 5LMS-PCL group was greater than that in the PCL group (Fig. 6H&J). Masson trichrome staining revealed extensive collagen deposition surrounding atrophied muscle fibers in the PCL group of rats, but little in other groups of rats (Fig. 6I&K). Together, these results indicate that implantation with the 5LMS-PCL NGC efficiently promoted motor function recovery and reduced structural damage in a rat model of sciatic nerve injury.

The enhanced motor function by the 5LMS-PCL NGC may stem from its function in improving the sciatic nerve regeneration. We explored the contribution of nerve myelination following 5LMS-PCL NGC implantation. Transmission electron microscopy (TEM) clearly exhibited a slightly larger axon diameter and a greater thickness in the myelin sheath in the regenerated nerves of rats in the 5LMS-PCL group, compared with those in the PCL group (Fig. 7A–C). Similar results were observed using H&E staining (Fig. 7D), and toluidine blue staining for myelination staining (Fig. 7E and F). Additionally, significant more $CD31^{+}$ vessels were observed closed to the newly-formed nerve fibers in the 5LMS-PCL group (Fig. 7G&H), an indicative of the pro-angiogenesis function of the 5LMS-PCL NGC.

Immunofluorescent staining revealed that compared with that in the PCL group of rats, the expression of PMP22 was up-regulated, but NCAM expression surrounding the nerve fibers was down-regulated in the 5LMS-PCL group of rats (Fig. 8A, D, E). Furthermore, a significantly higher proportion of active β-catenin-expressing S100+ SCs was observed in the 5LMS-PCL group (Fig. 8B, F). Further immunofluorescence displayed that the expression of NF200 increased in both the transverse and longitudinal sections of the newly generated sciatic nerves in the 5LMS-PCL group of rats at 4 weeks post-surgery (Fig. 8C, G, H). Interestingly, there was no significant difference in the numbers of S100+ SCs among these groups of rats. Therefore, implantation with the 5LMS-PCL NGCs promoted nerve regeneration and myelination *in vivo*.

4. Discussion

Biomaterial-based NGCs can provide a nerve repair-supportive and immunomodulatory microenvironment for the treatment of PNI when autologous nerve graft is unavailable. In the present study, we prepared LMS bioceramic particles and LMS-containing NGCs by incorporating LMS into PCL scaffolds. Functionally, LMS bioceramics were able to promote the proliferation, migration and myelination of SCs in a β-catenin-dependent manner. Furthermore, LMS bioceramics effectively recruited macrophages to promote their polarization towards pro-regenerative M2 cells and modulate the post-injury microenvironment for the remyelination of SCs, and the functional recovery and regeneration of injured nerves (Schematic graph). These findings suggest that

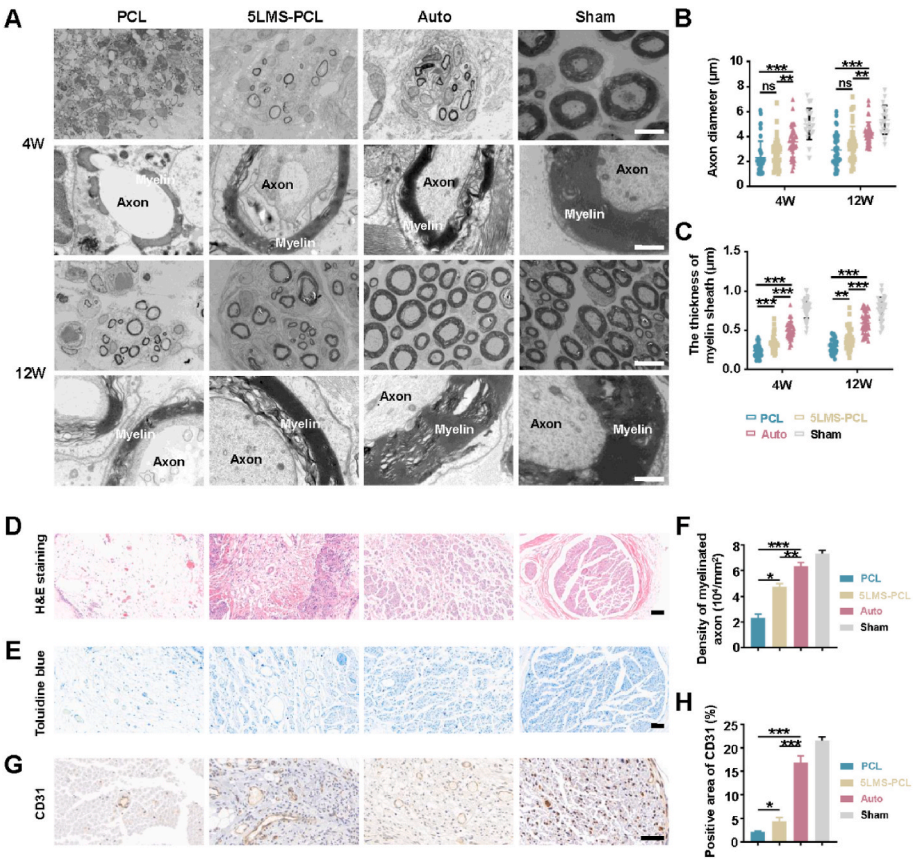

Fig. 7. LMS-containing NGCs promotes nerve regeneration *in vivo*.
(A–C) TEM images of axon diameter and myelin sheath thickness of regenerating nerves in each group of rats at 12 weeks post-surgery. Scale bars = 10, 1, 10 and 1 μm, respectively.
(D) Representative H&E staining images in each group. Scale bars = 50 μm.
(E & F) Toluidine blue staining and quantitative analysis of myelination. Scale bars = 50 μm.
(G & H) Representative images of immunohistochemical staining and quantitative analysis of the $CD31^{+}$ areas around regenerating nerves. Scale bars = 50 μm.

the LMS-containing NGCs may be potential biomaterials for immunomodulating peripheral nerve regeneration, and implantation with LMS-containing NGCs may be a new strategy for promoting nerve regeneration in clinical applications.

It is reported that loading some neurocytokines, such as ciliary neurotrophic factors (CNTF), basic fibroblast growth factors (bFGF), brain-derived neurotrophic factors (BDNF) and immunomodulatory factors (e.g., IL-4) to NGCs can regulate the injury microenvironment to accelerate the functional recovery of damaged nerves [7,46,47]. However, these cytokines are easily degraded and inactivated by endogenous enzymes within a short period. Therefore, it is impossible to maintain an optimal long-term modulatory effects during the entire process of tissue repair. Unlike biological cytokines, inorganic bioactive ions in biomaterial-based NGCs can be released from biomaterial scaffolds along with the degradation process [32,34]. Furthermore, they are stable in harsh conditions at injured sites. Hence, incorporating bioactive elements into NGCs has been a feasible strategy to manipulate the microenvironment of immune response and tissue regeneration [33,35]. Taken advantages of the biological effects of Li, Mg and Si elements on immunomodulation and nerve regeneration, LMS bioceramic nanoparticles were incorporated into NGCs to endow them with dual bioactivities for peripheral nerve regeneration. In addition, the matrix materials for fabricating the NGC should have high safety profile for potential clinic translation. The PCL-based NGC was approved by FDA and has been widely used as a scaffold in the clinic, holding many advantages [6,48]. PCL can be completely absorbed and its degradation products have low inflammatory activity. Functionally, it can mimic the endogenous epineurium for permitting nutrient and metabolic waste exchanges, while suppressing inflammatory cell infiltration surrounding the injured tissues. Its flexibility and elasticity are conducive for surgical suturing of the nerves. Besides its free of biological components, PCL has a high material processability and product reproducibility, easy for storage and sterilization for clinical applications [6,14,48].

Individual Li, Mg and Si ions have been reported to be beneficial to peripheral nerve regeneration. Li ions are widely employed in neuropsychiatric drugs, and have been shown to support both central and peripheral nerve regeneration [23,24,49,50] by modulating the WNT signaling [51–53]. Likewise, Mg ions can stimulate the peripheral sensory nerves [27] to promote nerve regeneration [25,54]. However, the *in vivo* effects and the underlying mechanisms have yet to be clarified. Silicon is commonly used as a base material for nerve conduits because of its poorly electrical conductivity but excellent biocompatibility [55]. In the current study, LMS-containing scaffolds exhibited continuous and sustained release of Li, Mg and Si ions with limited cytotoxicity against SCs. We are interested in further exploring the specific contribution of each type of ions to the repair-supportive microenvironment provided by the LMS-containing scaffolds, which may help in optimizing the production of the inorganic bioceramic biomaterials.

PNI usually induce the degradation of damaged axons, which activates Wallerian degeneration (WD), leading to SCs de-differentiation [10,56,57]. Subsequently, SCs can be subjected to adaptive intracellular reprogramming to become nerve repair cells [11,58,59]. These repair SCs secrets neurotrophins and undergo a dynamic differentiational process from a proliferative, un-myelinating phenotype to re-myelinating phenotype during this peripheral nerve regeneration [15–17]. How to manage these different phenotypes to contribute to the process of peripheral nerve regeneration is critical [60,61]. In the initial post-injury phase, SCs transdifferentiate from their myelinating phenotype to repair cells that express a lower level of myelin protein and higher levels of cell adhesion molecules, growth factors and their receptors [62,63]. In this stage of the nerve repair process, SCs can proliferate and migrate to form a bridge connecting the two ends of the injured nerves, together with increasing the NOTCH signaling [64]. In the later stage of nerve regeneration, SCs undergo remyelination to support the nerve repair, depending on the enhanced WNT/β-catenin signaling [65]. In the current study, we found that LMS-containing

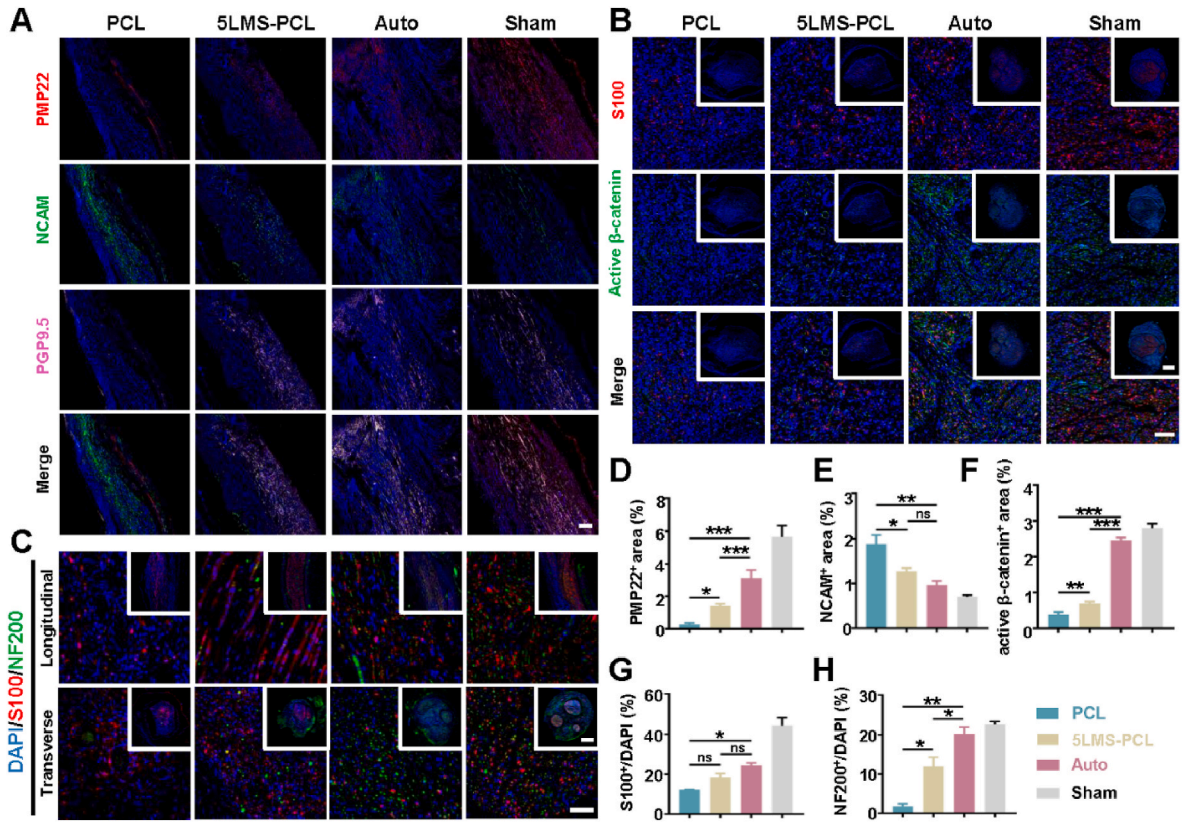

Fig. 8. LMS-containing NGCs promote nerve myelination and β-catenin activation *in vivo*.
(A) Representative immunofluorescent images of myelination in the regenerating nerves using anti-PMP22 (red) and anti-NCAM (green) as well as PGP 9.5 and DAPI. Scale bars = 100 μm.
(B) Representative immunofluorescent images of active β-catenin (green) expression in the regenerating nerves. Scale bars = 100 and 50 μm.
(C) Representative immunofluorescent images of the longitudinal and transverse sections of regenerating nerves using anti-NF200 (green) and anti-S100 (red) at 12 weeks post-surgery. Scale bars = 100 and 50 μm.
(D–H) Quantitative analysis of PMP22, NCAM, active β-catenin, NF200 and S100 expression in each group of rats.

scaffolds promoted the myelination of SCs in an active β-catenin-dependent manner. Notably, treatment with the LMS bioceramic particles enhanced the myelination of RSC96 cells and increased β-catenin activation with minimal effect on the proliferation and migration of RSC96 cells. These, to a large extent, are critical for maintaining a dynamic but balanced repair-supportive microenvironment. Given that active β-catenin is important for the myelination of SCs, further studies are necessary to investigate the effects of modulating β-catenin activity on nerve regeneration. Furthermore, it is also important to understand how the Notch and WNT signaling contribute to the myelination of SCs during the peripheral nerve injury.

Recent studies have highlighted the great significance of modulating the host immune response in promoting tissue regeneration [14,59,66,67]. Importantly, macrophages, as the major infiltrates, are found to be rapidly recruited into the NGCs [14,66,68,69]. Macrophage polarization refers that macrophages can be classically or alternatively activated into pro-inflammatory M1 or anti-inflammatory M2-like cells, reflecting their plasticity [70]. The M1 and M2 macrophages represent extremes of a continuum of activation states in a universe of adaptive responses [70–72]. However, due to the dynamic and stimulus dependence of macrophage phenotypes, it is usually difficult to capture the full spectrum of activated macrophages using molecular markers. Fortunately, scRNA-seq technology can profile specific cells in a mixed cell population at a single-cell level [73–75]. Recently, the scRNA-seq has been widely used to reveal immune characteristics [73,74,76,77]. In this study, we employed scRNA-seq to characterize different types of macrophages in the lesions of sciatic nerve injury following implantation with the LMS-containing NGCs. Our findings revealed that compared with the control PCL NGC, implantation with the LMS-contained NSCs promoted the accumulation of M2-like cells in the lesions of rats. It has been widely acknowledged that the M2-like macrophage plays a non-negligible role in peripheral nerve regeneration [78–80]. Our data show that the M2-like macrophage can promote the differentiation of SCs into a repair-supportive state, therefore contributing indirectly to peripheral nerve regeneration. The modulation of macrophage-SC interactions for peripheral nerve regeneration has now been a bourgeoning field [78]. Consistently, we found that macrophages migrated into the nerve bridge prior to SCs following the sciatic nerve injury in rats, particularly in the rats receiving the LMS-containing NGCs. It is possible that the LMS-containing NGCs may promote the migration of macrophages that adhered on NGC subsequently to facilitate the migration and differentiation of SCs. Moreover, the signals in the microenvironment can also feedback promote the reprogramming of metabolism, leading to the *trans*-differentiation of polarized macrophages toward M2-like cells. These M2-like macrophages can secret cytokines and NGFs, and also remodel the extracellular matrix to regulate the microenvironment for nerve regeneration [59,81,82]. Actually, we observed that implantation with the LMS-containing NGCs achieved a better outcome of nerve regeneration in rats, accompanied by a high M2/M1 ratio in the nerve bridge during the early graft period. These data were consistent with previous findings that the frequency or number of M2-like macrophages is associated positively with the number of regenerated axons [14,82]. These findings also support the notion that the M2-like cells modulate the microenvironment to promote the healing and remyelination by secreting several types of NGFs. Therefore, our findings may provide new evidence to demonstrate the potential therapeutic effect of the

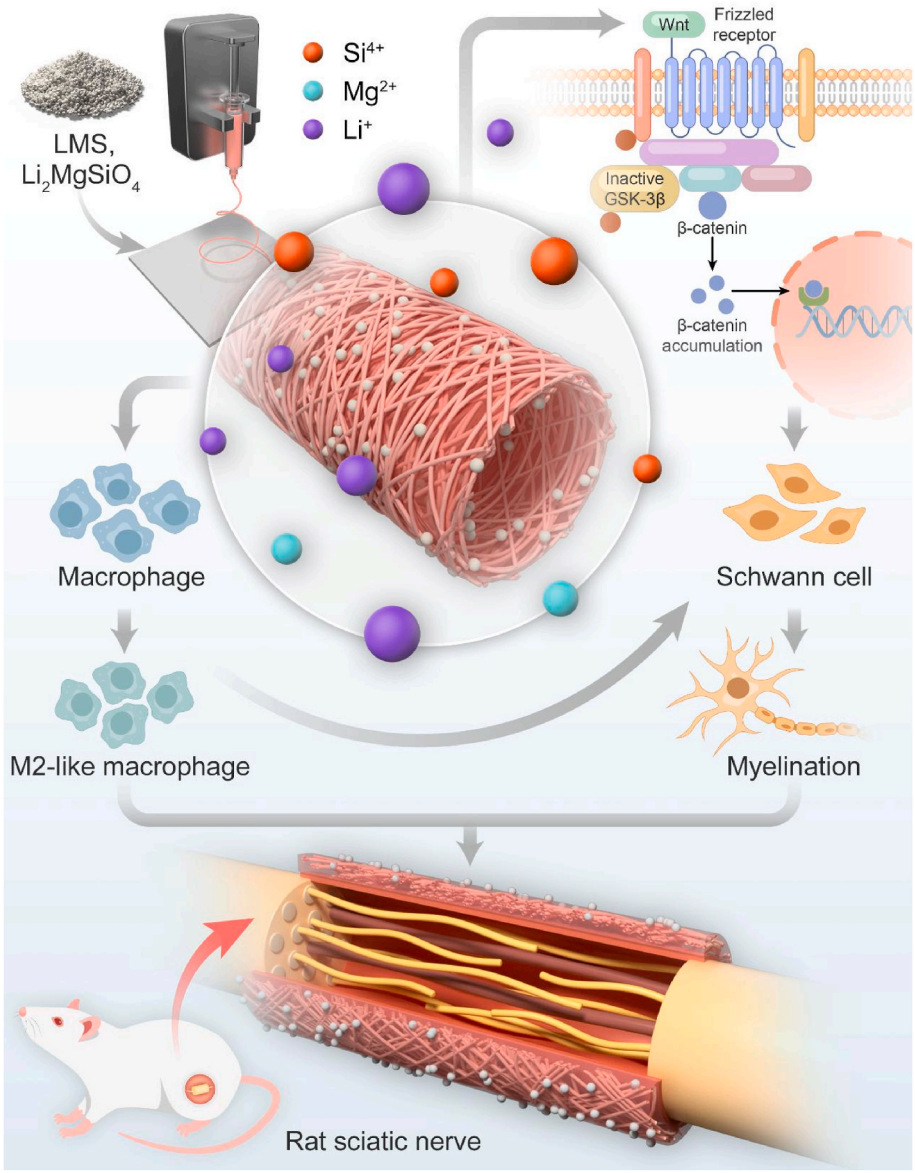

Schematic. 1. A schematic illustration of proposed mechanisms for LMS-containing nerve guidance conduit providing a dynamic immuno-modulatory and repair-supportive microenvironment for peripheral nerve regeneration.

LMS-containing NSCs on promoting nerve repair and regeneration *in vivo*. Further investigation of the molecular mechanisms underlying the action of the LMS-containing NSCs in promoting M2-like cell polarization and nerve regeneration will be intriguing.

5. Conclusion

In summary, our data indicated that LMS-containing NGCs effectively promoted M2-like macrophage polarization, SCs differentiation and peripheral nerve regeneration in vitro and *in vivo*. Mechanistically, the inorganic LMS bioceramics modulated the nerve injury environment into a repair-supportive microenvironment for peripheral nerve regeneration by promoting the differentiation of SCs towards a remyelination-state, up-regulating the expression of neurotrophic factors in a β-catenin-dependent manner. Furthermore, the LMS bioceramics modulated the immune microenvironment by recruiting pro-regenerative M2-like macrophages and/or promoting M2-like macrophage polarization, enhancing the migration and proliferation of SCs. Our study reveals inorganic bioceramics as promising biomaterials for supporting peripheral nerve regeneration, and provides preclinical evidence for using LMS-containing scaffolds to treat peripheral nerve regeneration.

Ethics approval and consent to participate

All animal experiments were performed after the approvement of the Animal Experimental Ethics Committee of Shanghai Ninth People's Hospital, Shanghai Jiao Tong University School of Medicine and complied with the requirements of the National Institutes of Health Guide for the Care and Use of Laboratory Animals.

CRediT authorship contribution statement

Yiting Sun: Conceptualization, Methodology, Formal analysis, Validation, Investigation, Writing – original draft. **Hongjian Zhang:** Methodology, Validation. **Yu Zhang:** Methodology, Validation, Formal analysis, Writing – review & editing, Funding acquisition. **Zheqi Liu:** Methodology, Formal analysis, Funding acquisition. **Dongming He:** Methodology, Formal analysis. **Wanlin Xu:** Methodology, Formal analysis. **Siyi Li:** Formal analysis, Validation. **Chenping Zhang:** Conceptualization, Data curation, Supervision. **Zhen Zhang:**

Conceptualization, Formal analysis, Data curation, Writing – review & editing, Funding acquisition, Supervision.

Declaration of competing interest

All the authors have no conflict of interests.

Acknowledgements

This work was supported by a grant from the National Natural Science Foundation of China (81900968), Shanghai Sailing Program (20YF1409900) and Shanghai Anticancer Association EYAS PROJECT (SACA- CY21A01 and SACA-CY22A01).

Appendix A. Supplementary data

Supplementary data to this article can be found online at https://doi.org/10.1016/j.bioactmat.2023.05.013.

References

[1] S. Behtaj, J.A. St John, J.A.K. Ekberg, M. Rybachuk, Neuron-fibrous scaffold interfaces in the peripheral nervous system: a perspective on the structural requirements, Neural regeneration research 17 (9) (2022) 1893–1897, https://doi.org/10.4103/1673-5374.329003.

[2] V.K. Singh, A. Haq, M. Tiwari, A.K. Saxena, Approach to management of nerve gaps in peripheral nerve injuries, Injury 53 (4) (2022) 1308–1318, https://doi.org/10.1016/j.injury.2022.01.031.

[3] J. Scheib, A. Hoke, Advances in peripheral nerve regeneration, Nat. Rev. Neurol. 9 (12) (2013) 668–676, https://doi.org/10.1038/nrneurol.2013.227.

[4] K. Liu, L. Yan, R. Li, Z. Song, J. Ding, B. Liu, X. Chen, 3D printed personalized nerve guide conduits for precision repair of peripheral nerve defects, Adv. Sci. 9 (12) (2022), e2103875, https://doi.org/10.1002/advs.202103875.

[5] S. Bassilios Habre, G. Bond, X.L. Jing, E. Kostopoulos, R.D. Wallace, P. Konofaos, The surgical management of nerve gaps: present and future, Ann. Plast. Surg. 80 (3) (2018) 252–261, https://doi.org/10.1097/SAP.0000000000001252.

[6] B.J. Parker, D.I. Rhodes, C.M. O'Brien, A.E. Rodda, N.R. Cameron, Nerve guidance conduit development for primary treatment of peripheral nerve transection injuries: a commercial perspective, Acta Biomater. 135 (2021) 64–86, https://doi.org/10.1016/j.actbio.2021.08.052.

[7] J. Moskow, B. Ferrigno, N. Mistry, D. Jaiswal, K. Bulsara, S. Rudraiah, S. G. Kumbar, Review: bioengineering approach for the repair and regeneration of peripheral nerve, Bioact. Mater. 4 (1) (2019) 107–113, https://doi.org/10.1016/j.bioactmat.2018.09.001.

[8] S. Vijayavenkataraman, Nerve guide conduits for peripheral nerve injury repair: a review on design, materials and fabrication methods, Acta Biomater. 106 (2020) 54–69, https://doi.org/10.1016/j.actbio.2020.02.003.

[9] C.R. Carvalho, J.M. Oliveira, R.L. Reis, Modern trends for peripheral nerve repair and regeneration: beyond the hollow nerve guidance conduit, Front. Bioeng. Biotechnol. 7 (2019) 337, https://doi.org/10.3389/fbioe.2019.00337.

[10] K.R. Jessen, R. Mirsky, The repair Schwann cell and its function in regenerating nerves, The Journal of physiology 594 (13) (2016) 3521–3531, https://doi.org/10.1113/JP270874.

[11] K.R. Jessen, P. Arthur-Farraj, Repair Schwann cell update: adaptive reprogramming, EMT, and stemness in regenerating nerves, Glia 67 (3) (2019) 421–437, https://doi.org/10.1002/glia.23532.

[12] P. Chen, X. Piao, P. Bonaldo, Role of macrophages in Wallerian degeneration and axonal regeneration after peripheral nerve injury, Acta Neuropathol. 130 (5) (2015) 605–618, https://doi.org/10.1007/s00401-015-1482-4.

[13] Q. Guo, H. Zhu, H. Wang, P. Zhang, S. Wang, Z. Sun, S. Li, C. Xue, X. Gu, S. Cui, Transcriptomic landscapes of immune response and axonal regeneration by integrative analysis of molecular pathways and interactive networks post-sciatic nerve transection, Front. Neurosci. 12 (2018) 457, https://doi.org/10.3389/fnins.2018.00457.

[14] X. Dong, S. Liu, Y. Yang, S. Gao, W. Li, J. Cao, Y. Wan, Z. Huang, G. Fan, Q. Chen, H. Wang, M. Zhu, D. Kong, Aligned microfiber-induced macrophage polarization to guide schwann-cell-enabled peripheral nerve regeneration, Biomaterials 272 (2021), 120767, https://doi.org/10.1016/j.biomaterials.2021.120767.

[15] K. Jessen, R. Mirsky, Schwann cells and their precursors emerge as major regulators of nerve development, Trends in neurosciences 22 (9) (1999) 402–410, https://doi.org/10.1016/s0166-2236(98)01391-5.

[16] Z. Chen, W. Yu, S. Strickland, Peripheral regeneration, Annu. Rev. Neurosci. 30 (2007) 209–233, https://doi.org/10.1146/annurev.neuro.30.051606.094337.

[17] G. Nocera, C. Jacob, Mechanisms of Schwann cell plasticity involved in peripheral nerve repair after injury, Cell. Mol. Life Sci. : CMLS 77 (20) (2020) 3977–3989, https://doi.org/10.1007/s00018-020-03516-9.

[18] C. Taveggia, M. Feltri, L. Wrabetz, Signals to promote myelin formation and repair, Nat. Rev. Neurol. 6 (5) (2010) 276–287, https://doi.org/10.1038/nrneurol.2010.37.

[19] S. Kargozar, R.K. Singh, H.W. Kim, F. Baino, "Hard" ceramics for "Soft" tissue engineering: paradox or opportunity? Acta Biomater. 115 (2020) 1–28, https://doi.org/10.1016/j.actbio.2020.08.014.

[20] E. Ochoa, Lithium as a neuroprotective agent for bipolar disorder: an overview, Cell. Mol. Neurobiol. 42 (1) (2022) 85–97, https://doi.org/10.1007/s10571-021-01129-9.

[21] R. Lenox, L. Wang, Molecular basis of lithium action: integration of lithium-responsive signaling and gene expression networks, Mol. Psychiatr. 8 (2) (2003) 135–144, https://doi.org/10.1038/sj.mp.4001306.

[22] J. Izsak, H. Seth, M. Iljin, S. Theiss, H. Agren, K. Funa, L. Aigner, E. Hanse, S. Illes, Differential acute impact of therapeutically effective and overdose concentrations of lithium on human neuronal single cell and network function, Transl. Psychiatry 11 (1) (2021) 281, https://doi.org/10.1038/s41398-021-01399-3.

[23] Y. Bu, X. Wang, L. Li, X. Hu, D. Tan, Z. Li, M. Lai, X. Qiu, F. Sun, H. Wang, F. Yang, D. Wu, J. Guo, Lithium loaded octa-poly(ethylene glycol) based adhesive facilitates axon regeneration and reconnection of transected peripheral nerves, Advanced healthcare materials 9 (13) (2020), e2000268, https://doi.org/10.1002/adhm.202000268.

[24] Y.C. Lin, S.J. Oh, K.G. Marra, Synergistic lithium chloride and glial cell line-derived neurotrophic factor delivery for peripheral nerve repair in a rodent sciatic nerve injury model, Plast. Reconstr. Surg. 132 (2) (2013) 251e–262e, https://doi.org/10.1097/PRS.0b013e31829588cf.

[25] J. Zhang, B. Zhang, J. Zhang, W. Lin, S. Zhang, Magnesium promotes the regeneration of the peripheral nerve, Front. Cell Dev. Biol. 9 (2021), 717854, https://doi.org/10.3389/fcell.2021.717854.

[26] Li Ye, J. Xu, J. Mi, X. He, Q. Pan, L. Zheng, H. Zu, Z. Chen, B. Dai, X. Li, Q. Pang, L. Zou, L. Zhou, L. Huang, W. Tong, G. Li, L. Qin, Biodegradable magnesium combined with distraction osteogenesis synergistically stimulates bone tissue regeneration via CGRP-FAK-VEGF signaling axis, Biomaterials 275 (2021), 120984, https://doi.org/10.1016/j.biomaterials.2021.120984.

[27] Y. Zhang, J. Xu, Y. Ruan, M. Yu, M. O'Laughlin, H. Wise, D. Chen, L. Tian, D. Shi, J. Wang, S. Chen, J. Feng, D. Chow, X. Xie, L. Zheng, L. Huang, S. Huang, K. Leung, N. Lu, L. Zhao, H. Li, D. Zhao, X. Guo, K. Chan, F. Witte, H. Chan, Y. Zheng, L. Qin, Implant-derived magnesium induces local neuronal production of CGRP to improve bone-fracture healing in rats, Nature medicine 22 (10) (2016) 1160–1169, https://doi.org/10.1038/nm.4162.

[28] L. Chen, C. Deng, J. Li, Q. Yao, J. Chang, L. Wang, C. Wu, 3D printing of a lithium-calcium-silicate crystal bioscaffold with dual bioactivities for osteochondral interface reconstruction, Biomaterials 196 (2019) 138–150, https://doi.org/10.1016/j.biomaterials.2018.04.005.

[29] L. Liu, Y. Liu, C. Feng, J. Chang, R. Fu, T. Wu, F. Yu, X. Wang, L. Xia, C. Wu, B. Fang, Lithium-containing biomaterials stimulate bone marrow stromal cell-derived exosomal miR-130a secretion to promote angiogenesis, Biomaterials 192 (2019) 523–536, https://doi.org/10.1016/j.biomaterials.2018.11.007.

[30] C. Qin, J.G. Ma, L. Chen, H.S. Ma, H. Zhuang, M. Zhang, Z.G. Huan, J. Chang, N. Ma, C.T. Wu, 3D bioprinting of multicellular scaffolds for osteochondral regeneration, Mater. Today 49 (2021) 68–84, https://doi.org/10.1016/j.mattod.2021.04.016.

[31] Z. Chen, A. Bachhuka, F. Wei, X. Wang, G. Liu, K. Vasilev, Y. Xiao, Nanotopography-based strategy for the precise manipulation of osteoimmunomodulation in bone regeneration, Nanoscale 9 (46) (2017) 18129–18152, https://doi.org/10.1039/c7nr05913b.

[32] Z. Chen, L. Chen, R. Liu, Y. Lin, S. Chen, S. Lu, Z. Lin, Z. Chen, C. Wu, Y. Xiao, The osteoimmunomodulatory property of a barrier collagen membrane and its manipulation via coating nanometer-sized bioactive glass to improve guided bone regeneration, Biomater. Sci. 6 (5) (2018) 1007–1019, https://doi.org/10.1039/c7bm00869d.

[33] Y. Huang, C. Wu, X. Zhang, J. Chang, K. Dai, Regulation of immune response by bioactive ions released from silicate bioceramics for bone regeneration, Acta Biomater. 66 (2018) 81–92, https://doi.org/10.1016/j.actbio.2017.08.044.

[34] W. Liu, J. Li, M. Cheng, Q. Wang, K.W.K. Yeung, P.K. Chu, X. Zhang, Zinc-Modified sulfonated polyetheretherketone surface with immunomodulatory function for guiding cell fate and bone regeneration, Adv. Sci. 5 (10) (2018), 1800749, https://doi.org/10.1002/advs.201800749.

[35] X.T. He, X. Li, M. Zhang, B.M. Tian, L.J. Sun, C.S. Bi, D.K. Deng, H. Zhou, H.L. Qu, C. Wu, F.M. Chen, Role of molybdenum in material immunomodulation and periodontal wound healing: targeting immunometabolism and mitochondrial function for macrophage modulation, Biomaterials 283 (2022), 121439, https://doi.org/10.1016/j.biomaterials.2022.121439.

[36] A. Bordbar-Khiabani, S. Bahrampour, M. Mozafari, M. Gasik, Surface functionalization of anodized tantalum with Mn3O4 nanoparticles for effective corrosion protection in simulated inflammatory condition, Ceram. Int. 48 (3) (2022) 3148–3156, https://doi.org/10.1016/j.ceramint.2021.10.088.

[37] W. Zhang, F. Zhao, D. Huang, X. Fu, X. Li, X. Chen, Strontium-substituted submicrometer bioactive glasses modulate macrophage responses for improved bone regeneration, ACS applied materials & interfaces 8 (45) (2016) 30747–30758, https://doi.org/10.1021/acsami.6b10378.

[38] H.R. Bakhsheshi-Rad, A.F. Ismail, M. Aziz, M. Akbari, Z. Hadisi, S.M. Khoshnava, E. Pagan, X. Chen, Co-incorporation of graphene oxide/silver nanoparticle into poly-L-lactic acid fibrous: a route toward the development of cytocompatible and antibacterial coating layer on magnesium implants, Mater Sci Eng C Mater Biol Appl 111 (2020), 110812, https://doi.org/10.1016/j.msec.2020.110812.

[39] H.R. Bakhsheshi-Rad, A.F. Ismail, M. Aziz, M. Akbari, Z. Hadisi, M. Omidi, X. Chen, Development of the PVA/CS nanofibers containing silk protein sericin as a wound dressing: in vitro and in vivo assessment, Int. J. Biol. Macromol. 149 (2020) 513–521, https://doi.org/10.1016/j.ijbiomac.2020.01.139.

[40] Z. Hadisi, M. Farokhi, H.R. Bakhsheshi-Rad, M. Jahanshahi, S. Hasanpour, E. Pagan, A. Dolatshahi-Pirouz, Y.S. Zhang, S.C. Kundu, M. Akbari, Hyaluronic acid (HA)-Based silk fibroin/zinc oxide core-shell electrospun dressing for burn wound management, Macromol. Biosci. 20 (4) (2020), e1900328, https://doi.org/10.1002/mabi.201900328.

[41] J. Hao, J. Zou, J. Zhang, K. Chen, D. Wu, W. Cao, G. Shang, J.Y.H. Yang, K. Wong-Lin, H. Sun, Z. Zhang, X. Wang, W. Chen, X. Zou, scSTAR reveals hidden heterogeneity with a real-virtual cell pair structure across conditions in single-cell RNA sequencing data, Briefings Bioinf. 24 (2) (2023), https://doi.org/10.1093/bib/bbad062.

[42] J. Du, J. Liu, S. Yao, H. Mao, J. Peng, X. Sun, Z. Cao, Y. Yang, B. Xiao, Y. Wang, P. Tang, X. Wang, Prompt peripheral nerve regeneration induced by a hierarchically aligned fibrin nanofiber hydrogel, Acta Biomater. 55 (2017) 296–309, https://doi.org/10.1016/j.actbio.2017.04.010.

[43] Q. Min, D. Parkinson, X. Dun, Migrating Schwann cells direct axon regeneration within the peripheral nerve bridge, Glia 69 (2) (2021) 235–254, https://doi.org/10.1002/glia.23892.

[44] M. Mahar, V. Cavalli, Intrinsic mechanisms of neuronal axon regeneration, Nature reviews, Neuroscience 19 (6) (2018) 323–337, https://doi.org/10.1038/s41583-018-0001-8.

[45] Y. Mao, X. Ge, C. Frank, J. Madison, A. Koehler, M. Doud, C. Tassa, E. Berry, T. Soda, K. Singh, T. Biechele, T. Petryshen, R. Moon, S. Haggarty, L. Tsai, Disrupted in schizophrenia 1 regulates neuronal progenitor proliferation via modulation of GSK3beta/beta-catenin signaling, Cell 136 (6) (2009) 1017–1031, https://doi.org/10.1016/j.cell.2008.12.044.

[46] Y. Cui, C. Lu, D. Meng, Z. Xiao, X. Hou, W. Ding, D. Kou, Y. Yao, B. Chen, Z. Zhang, J. Li, J. Pan, J. Dai, Collagen scaffolds modified with CNTF and bFGF promote facial nerve regeneration in minipigs, Biomaterials 35 (27) (2014) 7819–7827, https://doi.org/10.1016/j.biomaterials.2014.05.065.

[47] Y. Zhang, C. Lin, Z. Liu, Y. Sun, M. Chen, Y. Guo, W. Liu, C. Zhang, W. Chen, J. Sun, R. Xia, Y. Hu, X. Yang, J. Li, Z. Zhang, W. Cao, S. Sun, X. Wang, T. Ji, Cancer cells co-opt nociceptive nerves to thrive in nutrient-poor environments and upon nutrient-starvation therapies, Cell Metabol. 34 (12) (2022), https://doi.org/10.1016/j.cmet.2022.10.012.

[48] S. Kehoe, X.F. Zhang, D. Boyd, FDA approved guidance conduits and wraps for peripheral nerve injury: a review of materials and efficacy, Injury 43 (5) (2012) 553–572, https://doi.org/10.1016/j.injury.2010.12.030.

[49] Y. Bu, X. Wang, L. Li, X. Hu, D. Tan, Z. Li, M. Lai, X. Qiu, F. Sun, H. Wang, F. Yang, D. Wu, J. Guo, Lithium loaded octa-poly(ethylene glycol) based adhesive facilitates axon regeneration and reconnection of transected peripheral nerves, Advanced healthcare materials 9 (13) (2020), e2000268, https://doi.org/10.1002/adhm.202000268.

[50] A. Amerio, P. Ossola, F. Scagnelli, A. Odone, M. Allinovi, A. Cavalli, J. Iacopelli, M. Tonna, C. Marchesi, S.N. Ghaemi, Safety and efficacy of lithium in children and adolescents: a systematic review in bipolar illness, Eur. Psychiatr. : the journal of the Association of European Psychiatrists 54 (2018) 85–97, https://doi.org/10.1016/j.eurpsy.2018.07.012.

[51] T. da Silva, J. Eira, A. Lopes, A. Malheiro, V. Sousa, A. Luoma, R. Avila, R. Wanders, W. Just, D. Kirschner, M. Sousa, P. Brites, Peripheral nervous system plasmalogens regulate Schwann cell differentiation and myelination, J. Clin. Invest. 124 (6) (2014) 2560–2570, https://doi.org/10.1172/jci72063.

[52] H. Su, Q. Yuan, D. Qin, X. Yang, W. Wong, K. So, W. Wu, Lithium enhances axonal regeneration in peripheral nerve by inhibiting glycogen synthase kinase 3β activation, BioMed Res. Int. 2014 (2014), 658753, https://doi.org/10.1155/2014/658753.

[53] J. Makoukji, M. Belle, D. Meffre, R. Stassart, J. Grenier, G. Shackleford, R. Fledrich, C. Fonte, J. Branchu, M. Goulard, C. de Waele, F. Charbonnier, M.W. Sereda, E. E. Baulieu, M. Schumacher, S. Bernard, C. Massaad, Lithium enhances remyelination of peripheral nerves, Proc. Natl. Acad. Sci. U. S. A. 109 (10) (2012) 3973–3978, https://doi.org/10.1073/pnas.1121367109.

[54] L. Sun, M. Wang, S. Chen, B. Sun, Y. Guo, C. He, X. Mo, B. Zhu, Z. You, Molecularly engineered metal-based bioactive soft materials - neuroactive magnesium ion/polymer hybrids, Acta Biomater. 85 (2019) 310–319, https://doi.org/10.1016/j.actbio.2018.12.040.

[55] Y. Ma, K. Jiao, Q. Wan, J. Li, M. Liu, Z. Zhang, W. Qin, K. Wang, Y. Wang, F. Tay, L. Niu, in-situSilicified collagen scaffold induces semaphorin 3A secretion by sensory nerves to improve bone regeneration, Bioact. Mater. 9 (2022) 475–490, https://doi.org/10.1016/j.bioactmat.2021.07.016.

[56] G. Hussain, J. Wang, A. Rasul, H. Anwar, M. Qasim, S. Zafar, N. Aziz, A. Razzaq, R. Hussain, J.G. de Aguilar, T. Sun, Current status of therapeutic approaches against peripheral nerve injuries: a detailed story from injury to recovery, Int. J. Biol. Sci. 16 (1) (2020) 116–134, https://doi.org/10.7150/ijbs.35653.

[57] G. Nocera, C. Jacob, Mechanisms of Schwann cell plasticity involved in peripheral nerve repair after injury, Cell. Mol. Life Sci. : CMLS 77 (20) (2020) 3977–3989, https://doi.org/10.1007/s00018-020-03516-9.

[58] M. Mahar, V. Cavalli, Intrinsic mechanisms of neuronal axon regeneration, Nature reviews, Neuroscience 19 (6) (2018) 323–337, https://doi.org/10.1038/s41583-018-0001-8.

[59] J. Li, Y. Yao, Y. Wang, J. Xu, D. Zhao, M. Liu, S. Shi, Y. Lin, Modulation of the crosstalk between schwann cells and macrophages for nerve regeneration: a therapeutic strategy based on a multifunctional tetrahedral framework nucleic acids system, Advanced materials (2022), e2202513, https://doi.org/10.1002/adma.202202513.

[60] B. Liu, Y. Kong, W. Shi, M. Kuss, K. Liao, G. Hu, P. Xiao, J. Sankarasubramanian, C. Guda, X. Wang, Y. Lei, B. Duan, Exosomes derived from differentiated human ADMSC with the Schwann cell phenotype modulate peripheral nerve-related cellular functions, Bioact. Mater. 14 (2022) 61–75, https://doi.org/10.1016/j.bioactmat.2021.11.022.

[61] Q. Yang, S. Su, S. Liu, S. Yang, J. Xu, Y. Zhong, Y. Yang, L. Tian, Z. Tan, J. Wang, Z. Yu, Z. Shi, F. Liang, Exosomes-loaded electroconductive nerve dressing for nerve regeneration and pain relief against diabetic peripheral nerve injury, Bioact. Mater. 26 (2023) 194–215, https://doi.org/10.1016/j.bioactmat.2023.02.024.

[62] S. You, T. Petrov, P. Chung, T. Gordon, The expression of the low affinity nerve growth factor receptor in long-term denervated Schwann cells, Glia 20 (2) (1997) 87–100, https://doi.org/10.1002/(sici)1098-1136(199706)20:2<87::aid-glia1>3.0.co;2-1.

[63] M. Rahmatullah, A. Schroering, K. Rothblum, R. Stahl, B. Urban, D. Carey, Synergistic regulation of Schwann cell proliferation by heregulin and forskolin, Mol. Cell Biol. 18 (11) (1998) 6245–6252, https://doi.org/10.1128/mcb.18.11.6245.

[64] A. Woodhoo, M. Alonso, A. Droggiti, M. Turmaine, M. D'Antonio, D. Parkinson, D. Wilton, R. Al-Shawi, P. Simons, J. Shen, F. Guillemot, F. Radtke, D. Meijer, M. Feltri, L. Wrabetz, R. Mirsky, K. Jessen, Notch controls embryonic Schwann cell differentiation, postnatal myelination and adult plasticity, Nat. Neurosci. 12 (7) (2009) 839–847, https://doi.org/10.1038/nn.2323.

[65] G. Li, T. Zheng, L. Wu, Q. Han, Y. Lei, L. Xue, L. Zhang, X. Gu, Y. Yang, Bionic microenvironment-inspired synergistic effect of anisotropic micro-nanocomposite topology and biology cues on peripheral nerve regeneration, Sci. Adv. 7 (28) (2021), https://doi.org/10.1126/sciadv.abi5812.

[66] X. Dong, P. Wu, L. Yan, K. Liu, W. Wei, Q. Cheng, X. Liang, Y. Chen, H. Dai, Oriented nanofibrous P(MMD-co-LA)/Deferoxamine nerve scaffold facilitates peripheral nerve regeneration by regulating macrophage phenotype and revascularization, Biomaterials 280 (2022), 121288, https://doi.org/10.1016/j.biomaterials.2021.121288.

[67] J. Yu, Y. Lin, G. Wang, J. Song, U. Hayat, C. Liu, A. Raza, X. Huang, H. Lin, J. Y. Wang, Zein-induced immune response and modulation by size, pore structure and drug-loading: application for sciatic nerve regeneration, Acta Biomater. 140 (2022) 289–301, https://doi.org/10.1016/j.actbio.2021.11.035.

[68] A.L. Cattin, J.J. Burden, L. Van Emmenis, F.E. Mackenzie, J.J. Hoving, N. Garcia Calavia, Y. Guo, M. McLaughlin, L.H. Rosenberg, V. Quereda, D. Jamecna, I. Napoli, S. Parrinello, T. Enver, C. Ruhrberg, A.C. Lloyd, Macrophage-induced blood vessels guide schwann cell-mediated regeneration of peripheral nerves, Cell 162 (5) (2015) 1127–1139, https://doi.org/10.1016/j.cell.2015.07.021.

[69] X.P. Dun, L. Carr, P.K. Woodley, R.W. Barry, L.K. Drake, T. Mindos, S.L. Roberts, A. C. Lloyd, D.B. Parkinson, Macrophage-derived Slit3 controls cell migration and axon pathfinding in the peripheral nerve bridge, Cell Rep. 26 (6) (2019) 1458–1472 e4, https://doi.org/10.1016/j.celrep.2018.12.081.

[70] M. Locati, G. Curtale, A. Mantovani, Diversity, mechanisms, and significance of macrophage plasticity, Annual review of pathology 15 (2020) 123–147, https://doi.org/10.1146/annurev-pathmechdis-012418-012718.

[71] Z. Luo, B. Qi, Y. Sun, Y. Chen, J. Lin, H. Qin, N. Wang, R. Shi, X. Shang, S. Chen, J. Chen, Engineering bioactive M2 macrophage-polarized, anti-inflammatory, miRNA-based liposomes for functional muscle repair: from exosomal mechanisms to biomaterials, Small 18 (34) (2022), e2201957, https://doi.org/10.1002/smll.202201957.

[72] C. Bohaud, J. Cruz, C. Terraza, A. Barthelaix, B. Laplace-Builhe, C. Jorgensen, Y. Arribat, F. Djouad, Lactate metabolism coordinates macrophage response and regeneration in zebrafish, Theranostics 12 (8) (2022) 3995–4009, https://doi.org/10.7150/thno.65235.

[73] C. Li, A. Menoret, C. Farragher, Z. Ouyang, C. Bonin, P. Holvoet, A.T. Vella, B. Zhou, Single cell transcriptomics based-MacSpectrum reveals novel macrophage activation signatures in diseases, JCI insight 5 (2019), https://doi.org/10.1172/jci.insight.126453.

[74] C. Qie, J. Jiang, W. Liu, X. Hu, W. Chen, X. Xie, J. Liu, Single-cell RNA-Seq reveals the transcriptional landscape and heterogeneity of skin macrophages in Vsir(-/-) murine psoriasis, Theranostics 10 (23) (2020) 10483–10497, https://doi.org/10.7150/thno.45614.

[75] N. Johansen, G. Quon, scAlign: a tool for alignment, integration, and rare cell identification from scRNA-seq data, Genome Biol. 20 (1) (2019) 166, https://doi.org/10.1186/s13059-019-1766-4.

[76] P. Guo, X. Liu, P. Zhang, Z. He, Z. Li, M. Alini, R.G. Richards, S. Grad, M. J. Stoddart, G. Zhou, X. Zou, D. Chan, W. Tian, D. Chen, M. Gao, Z. Zhou, S. Liu, A single-cell transcriptome of mesenchymal stromal cells to fabricate bioactive hydroxyapatite materials for bone regeneration, Bioact. Mater. 9 (2022) 281–298, https://doi.org/10.1016/j.bioactmat.2021.08.009.

[77] W. Lin, Q. Li, D. Zhang, X. Zhang, X. Qi, Q. Wang, Y. Chen, C. Liu, H. Li, S. Zhang, Y. Wang, B. Shao, L. Zhang, Q. Yuan, Mapping the immune microenvironment for mandibular alveolar bone homeostasis at single-cell resolution, Bone research 9 (1) (2021) 17, https://doi.org/10.1038/s41413-021-00141-5.

[78] J. Li, Y. Yao, Y. Wang, J. Xu, D. Zhao, M. Liu, S. Shi, Y. Lin, Modulation of the crosstalk between schwann cells and macrophages for nerve regeneration: a therapeutic strategy based on a multifunctional tetrahedral framework nucleic acids system, Adv Mater 34 (46) (2022), e2202513, https://doi.org/10.1002/adma.202202513.

[79] R. Feng, V. Muraleedharan Saraswathy, M.H. Mokalled, V. Cavalli, Self-renewing macrophages in dorsal root ganglia contribute to promote nerve regeneration, Proc. Natl. Acad. Sci. U. S. A. 120 (7) (2023), e2215906120, https://doi.org/10.1073/pnas.2215906120.

[80] X. Gao, Z. Han, C. Huang, H. Lei, G. Li, L. Chen, D. Feng, Z. Zhou, Q. Shi, L. Cheng, X. Zhou, An anti-inflammatory and neuroprotective biomimetic nanoplatform for

repairing spinal cord injury, Bioact. Mater. 18 (2022) 569–582, https://doi.org/10.1016/j.bioactmat.2022.05.026.

[81] J.A. Stratton, P.T. Shah, Macrophage polarization in nerve injury: do Schwann cells play a role? Neural regeneration research 11 (1) (2016) 53–57, https://doi.org/10.4103/1673-5374.175042.

[82] Z. Msheik, M. El Massry, A. Rovini, F. Billet, A. Desmouliere, The macrophage: a key player in the pathophysiology of peripheral neuropathies, J. Neuroinflammation 19 (1) (2022) 97, https://doi.org/10.1186/s12974-022-02454-6.